An Analytical Framework for Stress Shadow Analysis During Hydraulic Fracturing - Applied to the Bakken Formation, Saskatchewan, Canada

Mostafa Gorjian[1], Sepidehalsadat Hendi[1], Christopher D. Hawkes[2]

[1]Geological Engineering, Department of Earth, Ocean and Atmospheric Sciences, University of British Columbia, Vancouver, BC, Canada

[2]Geological Engineering, Department of Civil, Geological, and Environmental Engineering, University of Saskatchewan, Saskatoon, SK, Canada

Correspondence to: Mostafa Gorjian (mgorjian@eoas.ubc.ca), Christopher D. Hawkes (cdh780@mail.usask.ca)

Abstract. This paper presents selected results of a broader research project pertaining to the hydraulic fracturing of oil reservoirs hosted in the siltstones and fine grained sandstones of the Bakken Formation in southeast Saskatchewan, Canada. The Bakken Formation contains significant volumes of hydrocarbon, but large-scale hydraulic fracturing is required to achieve economic production rates. The performance of hydraulic fractures is strongly dependent on fracture attributes such as length and width, which in turn are dependent on in-situ stresses.

This paper reviews methods for estimating changes to the in-situ stress field (stress shadow) resulting from mechanical effects (fracture opening), poro-elastic effects, and thermo-elastic effects associated with fluid injection for hydraulic fracturing. The application of this method is illustrated for a multi-stage hydraulic fracturing operation, to predict principal horizontal stress magnitudes and orientations at each stage. A methodology is also presented for using stress shadow models to assess the potential for inducing shear failure on natural fractures.

The results obtained in this work suggest that thermo and poro-elastic stresses are negligible for hydraulic fracturing in the Bakken Formation of southeast Saskatchewan, hence a mechanical stress shadow formulation is used for analyzing multistage hydraulic fracture treatments. This formulation (and a simplified version of the formulation) predicts an increase in instantaneous shut-in pressure (ISIP) that is consistent with field observations (i.e., ISIP increasing from roughly 21.6 MPa to values slightly greater than 26 MPa) for a 30-stage fracture treatment. The size of predicted zones of shear failure on natural fractures are comparable with the event clouds observed in microseismic monitoring when assumed values of 115°/65° are used for natural fracture strike/dip; however, more data on natural fracture attributes and more microseismic monitoring data for the area are required before rigorous assessment of the model is possible.

1 Introduction

30 During fracturing operations, the changes in principal stress magnitudes and orientations induced in the reservoir during a given fracture stage may alter the conditions for the subsequent stages, giving rise to the so-called "stress shadow" effect (see Figure 1). Stress shadows can impact the effectiveness of fracturing operations by increasing the injection pressures required to create and propagate fractures, reducing fracture width, and potentially altering fracture trajectory (Nagel et al., 2013;

35 Zangeneh et al., 2015; Gorjian & Hawkes, 2017; Patterson, 2017; Roussel, 2017). The design of effective fracture stimulation treatments in a reservoir requires analysis of the geomechanical attributes of the reservoir and the prediction of stress shadow effects (Smith & Montgomery, 2015; Suppachoknirun and Tutuncu, 2017).

Analytical solutions exist for modeling stress shadows under idealized conditions (e.g., homogeneous and isotropic rock properties; linear elastic material behaviour; 2-dimensiontal, plane strain geometry). The following is a summary of stress

40 shadow mechanisms and the corresponding references for available analytical solutions. The equations drawn from literature and used in this work are presented in Section 2.

- Mechanical stress shadow; i.e., the stress increase caused by a fracture as it "pushes" outwards on the rock mass on either side of the fracture plane. A conceptual model for the mechanical stress shadow is given in Figure 2. General expressions for the resulting induced stress field were presented by Warpinski (1989), Pollard and Segall (1987), and

45 can also be found in Ge and Ghassemi (2008). The Gohfer software also calculates stress shadow by using a 1-D analytical solution for the point-load stress shadow presented by Boussinesq (1885).

- Poro-elastic stress shadow; i.e., increasing pore pressure due to fluid leak-off into the reservoir rock matrix causing dilation of the reservoir and consequently a reduction in fracture width. Equations for the resulting induced stress field were presented by Koning (1985), Perkins and Gonzalez (1985) and Ge and Ghasemi (2008).

50 - Thermo-elastic stress shadow; i.e., the stress reduction caused by reservoir contraction associated with temperature drop due to the use of a fracture fluid with temperature that is cooler (T_f) than the native reservoir temperature (T_R). Equations for the resulting induced stress field were presented by Perkins and Gonzalez (1985), and can also be found in Ge and Ghassemi (2008).

The main objective of this research was to develop a better understanding of the combined effects of mechanical, thermos- and

55 poro-elastic stress shadows during the process of hydraulic fracturing, with application to the Bakken Formation (a tight oil reservoir) in western Canada.

Pursuit of this objective was achieved by undertaking the following tasks:

- Developing analytical models for quantifying the effects of stress shadows, and using these models to analyse thermo-hydro-mechanical stress perturbation (stress shadow) around hydraulic fractures as a function of the reservoir depth,

60 in-situ stress ratio, wellbore spacing and injection rate.

- Testing the thermo-hydro-mechanical stress shadow model by comparing its results with field data.

The relatively simple stress shadow formulation developed in this project can be used easily on site to assess the effects of stage spacing on fracture pressure and (potentially) fracture orientation, improving fracture stimulation design.

The methodology developed in this work can also be extended to predict zones of possible rock failure (due to shearing) around a hydraulic fracture. If there is a large-scale discontinuity around the wellbore, failure on that discontinuity due to hydraulic fracture can be assessed and that assessment can mitigate the potential for operational problems due to reactivation. Predicting the failure zone associated with slip on smaller natural fractures around a hydraulic fracture is also valuable for predicting stimulated reservoir volume. As such, the following task was additional undertaken in this work:

- Using stress shadow modeling results to assess the potential for induced shear failure on natural fractures, as a means of predicting the dimensions of the microseismic cloud area around a hydraulic fracture.

2 Analytical Models for Stress Shadow Distribution

2.1 Workflow for Using Analytical Stress Shadow Models in Tandem with a Numerical Fracture Simulator

This section presents equations to analyze and calculate the stress shadow existing at each stage of hydraulic fracturing due to the cumulative effects of the previous stages. The workflow used to implement these stress shown models in combination with a numerical fracture simulator is shown in Figure 3. In this work, hydraulic fracture dimensions and pressures were predicted using the commercial fracture simulator GOHFER (Barree and associates, 2016).

The process begins by simulating the first fracture stage with GOHFER using the initial in-situ stress state as model input. The time interval simulated includes the injection period as well as the ensuing pressure falloff, up to the point in time when the second fracture stage is undertaken. At this point, key attributes of the fracture (length, average width, average pressure) are taken and used as inputs for the stress shadow equations. In turn, these equations provide estimates of stress changes induced at the location of the second fracturing stage, which are superimposed on the original in-situ stress state to yield a revised stress state. This revised stress state is used as input for a GOHFER simulation of the second fracture stage. The workflow is then repeated for each subsequent fracture stage, with the stress shadow effects of all preceding stages accounted for.

GOHFER was chosen for this work as a simulator. The rationale for this choice was based on the fact that this modeling tool strikes a balance between being physically robust (in terms of physical processes directly associated with hydraulic fracture behaviour) while being sufficiently practical and accessible to be widely used in the petroleum industry. As such, the results of this work would be relatable in form and content to industry personnel, and new insights and methods would have greater potential for being adopted in practice.

The following sections present the equations that have been identified to enable prediction of stress shadow are based on mechanical, thermal and poro-elastic mechanisms.
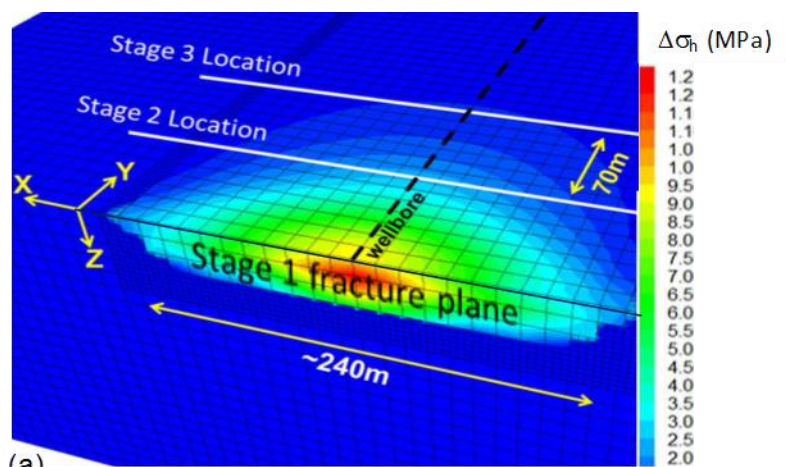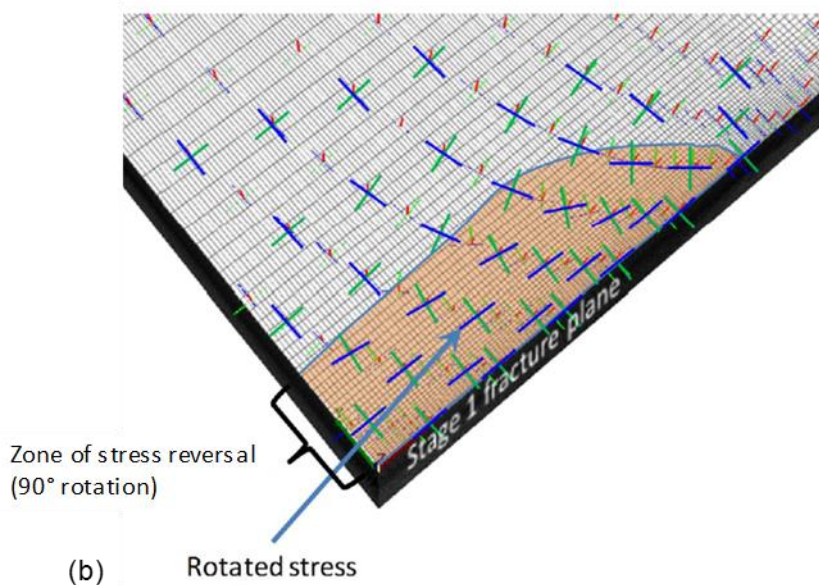
Figure 1: Scenarios Examples illustrating the stress shadow effect resulting from the creation of a hydraulic fracture: (a) Change in minimum horizontal stress magnitude ($\Delta\sigma_h$) resulting from the first fracture stage; and (b) orientations of maximum horizontal (green lines) and minimum horizontal (dark blue lines) stresses, for an extreme case in which stress reversal (90° stress rotation) occurs near the hydraulic fracture. (After Oilfield Geomechanics, 2015)

95
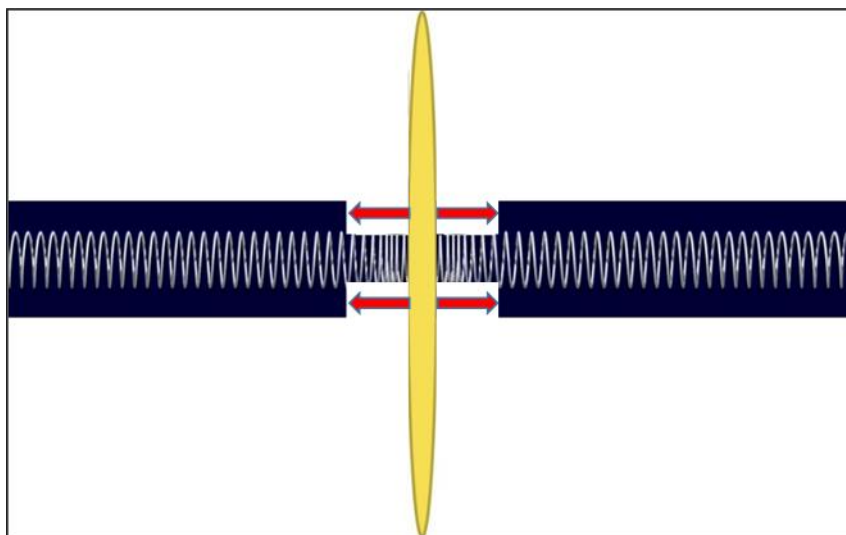
Figure 2: Conceptual model for mechanical stress shadow. As the fracture opens, it pushes outwards on rock mass on either side of the fracture plane and it may increase stress (Gorjian & Hawkes, 2017).
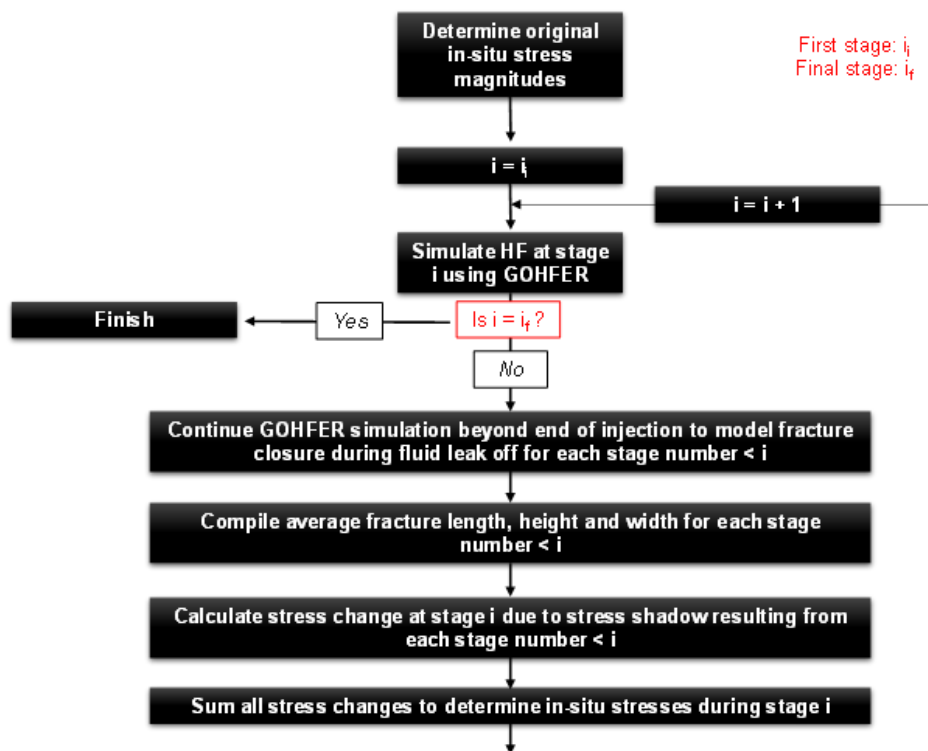
100

Figure 3: Algorithm which is applied for calculating stress shadow in multi-stage hydraulic fracturing (HF) treatment. i denotes stage number (varying from 1 to n), and HF denotes hydraulic fracture.

2.2 Mechanical Stress Shadow

For the calculation of mechanical stress shadow around a fracture, an improved version of the Pollard and Segall (1987) method
105 was used (Figure 4). Ge and Ghassemi (2008) have also used this technique. The hydraulic fracture is assumed to be a 2-D
crack with an average propped width of ϖ. The equations from Pollard and Segall (1987) are given in equations 1 to 9, as
follows.

$$\Delta\sigma_X = -\frac{2E'\varpi}{\pi h}\left[Rr^{-1}*\cos(\theta-\theta_{ave})-1-\left(L/_2\right)^2 Rr^{-3}\sin(\theta)\sin(3\theta_{ave}))\right]+(\tau_{XY} \tag{1}$$
$$-\tau_{XY}{}^c)\left[\left(L/_2\right)^2 Rr^{-3}\sin(\theta)\sin(3\theta_{ave})\right]$$

$$\Delta\sigma_Y = -\frac{2E'\varpi}{\pi h}\left[Rr^{-1}*\cos(\theta-\theta_{ave})-1+\left(L/_2\right)^2 Rr^{-3}\sin(\theta)\sin(3\theta_{ave}))\right]+(\tau_{XY} \tag{2}$$
$$-\tau_{XY}{}^c)\left[\left(L/_2\right)^2 Rr^{-3}\sin(\theta)\cos(3\theta_{ave})\right]$$

$$\Delta\tau_{XY} = (\tau_{XY}-\tau_{XY}{}^c)\left[Rr^{-1}*\cos(\theta-\theta_{ave})-1-\left(L/_2\right)^2 Rr^{-3}\sin(\theta)\sin(3\theta_{ave})\right] \tag{3}$$
$$-\frac{2E'\varpi}{\pi h}\left[\left(L/_2\right)^2 Rr^{-3}\sin(\theta)\cos(3\theta_{ave})\right]$$

And $\Delta\sigma_Z = \upsilon(\Delta\sigma_X+\Delta\sigma_Y)$ (4)

Where $R = \sqrt{X^2+Y^2}$, $\theta = tan^{-1}(Y/_X)$ (5)

$R_1 = \sqrt{Y^2+(L/_2-X)^2}$, $\theta_1 = tan^{-1}[Y/_{(X-L/_2)}]$ (6)

$R_2 = \sqrt{Y^2+(X+L/_2)^2}$, $\theta_2 = tan^{-1}[Y/_{(X+L/_2)}]$ (7)

r=$\sqrt{R_1 R_2}$, $\theta_{ave} = \frac{\theta_1+\theta_2}{2}$ (8)

τ_{xy} and $\tau_{xy}{}^c$ = in-situ shear stress and shear stress on the crack surface (assumed
zero because hydrostatic pressure of fracture fluid, inside of the crack, doesn't create
shear stress on the crack surface)

$\Delta\sigma_X$, $\Delta\sigma_Y$ and $\Delta\sigma_Z$ = induced stress in X, Y and Z directions.

$\Delta\tau_{XY}$ = induced shear stress in X-Y plane

$$E' = \frac{E}{(1-v^2)}$$

(9)

Negative values of angles θ, θ_1 and θ_2 (shown in Figure 3) should be corrected by adding 180° (π radians). Values for L and ϖ are taken from Gohfer simulation output for the prior hydraulic fracture stages.
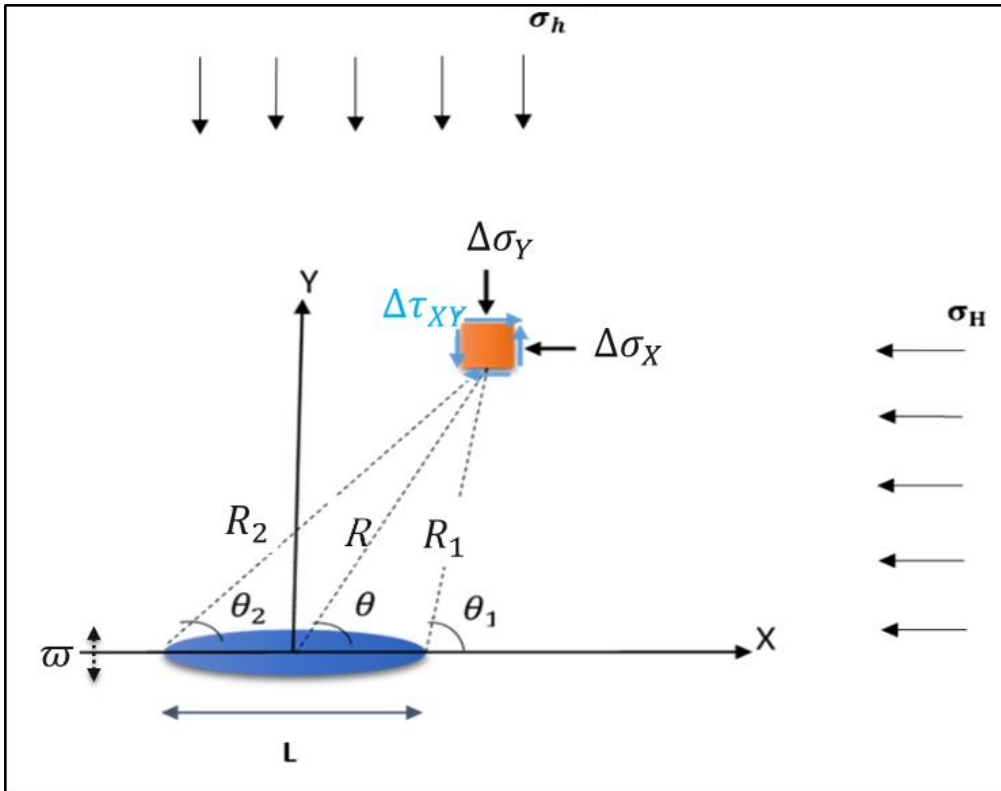
110

Figure 4: Induced mechanical stress around the fracture. The orange square represents an element volume of the formation and is exaggerated in dimensions for the purpose of stress visualization (after Ge & Ghassemi, 2008).

2.3 Thermo-elastic Stress Shadow

115 In Most studies in thermo-elastic stresses have been conducted in the field of geothermal production (Ge & Ghassemi, 2008). In the petroleum industry, the thermo-elastic stress shadow is often considered to be insignificant due to the small difference in temperature between the injected fluid and in-situ rock. As a result, it is assumed that temperature is distributed uniformly and elliptically around the fracture and that the rock temperature increases outwards as a fracture propagates and injection

continues. The cool region (i.e., rock within the ellipse of semi-axes a_0 and b_0 in Figure 5) is assumed to have the same
120   temperature as the injected fluid, and the unaffected region (i.e., rock exterior to the ellipse of semi-axes a_0 and b_0) remains
constant at the in-situ reservoir temperature.

For the cool region, thermo-elastic stresses perpendicular ($\Delta\sigma_{1T}$) and parallel ($\Delta\sigma_{2T}$) to the fracture surface are calculated as
follows (Perkins and Gonzales, 1985):

$$\frac{(1-v)\Delta\sigma_{1T}}{E\alpha\Delta T} = \frac{\left(b_0/a_0\right)}{1+\left(b_0/a_0\right)}$$
(10)

$$+ \left[\frac{1}{1+\left(b_0/a_0\right)}\right]\left(1 \Big/ \left\{1 + \frac{1}{2}\left[1.45\left(\frac{h}{2b_0}\right)^{0.9} + 0.35\left(\frac{h}{2b_0}\right)^2\right]\left[1 + \left(\frac{b_0}{a_0}\right)^{0.774}\right]\right\}\right)$$

$$\frac{(1-v)\Delta\sigma_{2T}}{E\alpha\Delta T} = \frac{\left(b_0/a_0\right)}{1+\left(b_0/a_0\right)}$$
(11)

$$+ \left[\frac{\left(b_0/a_0\right)}{1+\left(b_0/a_0\right)}\right]\left(1 \Big/ \left\{1 + \left[1.45\left(\frac{h}{2b_0}\right)^{0.9} + 0.35\left(\frac{h}{2b_0}\right)^2\right]\left[1 + \left(1 - \frac{b_0}{a_0}\right)^{1.36}\right]\right\}\right)$$

125

Where v = Poisson's ratio

E = Young's modulus

α_T = linear coefficient of thermal expansion

ΔT = the difference between fluid temperature (T_f) and reservoir temperature (T_R)

130   b_0 and a_0 = minor and major semi-axes of the cool region, respectively

h = height of fracture

$\Delta\sigma_{1T}$ and $\Delta\sigma_{2T}$ = thermo-elastic stress change perpendicular and parallel to fracture surface at any point around the
fracture

135   For calculating the semi-axes of the cool region, the following equations are used:

$$W_i = Qt$$
(12)

$$V_{wt} = W_i \Big/ (Phie(1 - S_{or} - S_{wi})) \qquad (13)$$

$$V_C = \frac{\rho_w C_w W_i}{\rho_{gr} C_{gr}(1 - Phie) + \rho_w C_w Phie(1 - S_{or}) + \rho_o C_o Phie S_{or}} \qquad (14)$$

$$F_1 = 2 * V_C \Big/ (\pi * h * L_f{}^2) + 0.5 * \sqrt{(\frac{4 V_C}{\pi L_f{}^2 h})^2 + 4} \qquad (15)$$

$$a_0 = L_f * (\sqrt{F_1} + \frac{1}{\sqrt{F_1}}) \Big/ 2 \qquad (16)$$

$$b_0 = L_f * (\sqrt{F_1} - \frac{1}{\sqrt{F_1}}) \Big/ 2 \qquad (17)$$

Where t = time of injection

Q = rate of injection

W_i = cumulative volume of fluid injected

140   V_c = volume of rock formation cooled by the injected fluid

F_1 = an intermediate calculation parameter

L_f = fracture half length

$Phie$ = effective porosity

S_{or} = residual oil saturation

145   S_{wi} = initial water saturation

ρ_{gr}, ρ_w and ρ_o = density of mineral grains, water and oil, respectively

C_{gr}, C_w and C_o = specific heat of mineral grains, water and oil, respectively
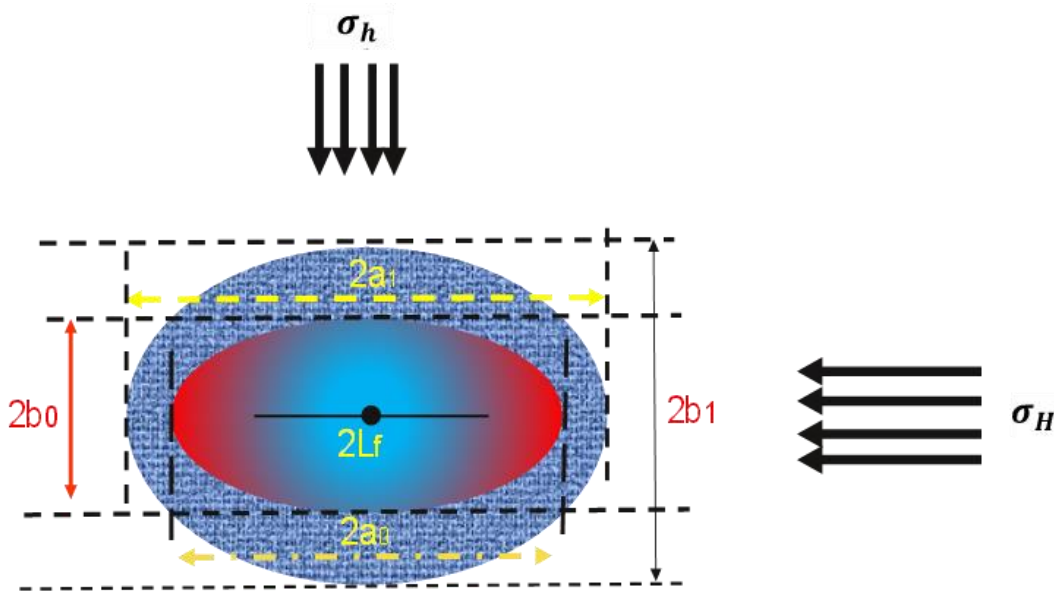
Figure 5: Cool region (ellipse of semi-axes a_0 and b_0) and flood region (semi-axes a_1 and b_1) around the fracture with half-length of L_f

150

2.4 Poro-elastic Stress Shadow

For the flood region zone (i.e., the rock within the ellipse of semi-axes of a_1 and b_1 in Figure 5), poro-elastic stresses perpendicular ($\Delta\sigma_{1p}$) and parallel ($\Delta\sigma_{2p}$) to the fracture surface are calculated as follows (Perkins and Gonzales, 1985):

155

$$\frac{(1-v)\Delta\sigma_{1p}}{EJ\Delta p} = \frac{\left(b_1/a_1\right)}{1+\left(b_1/a_1\right)} \tag{18}$$

$$+ \left[\frac{1}{1+\left(b_1/a_1\right)}\right]\left(1\Big/\left\{1+1/2\left[1.45\left(\frac{h}{2b_1}\right)^{0.9}+0.35\left(\frac{h}{2b_1}\right)^2\right]\left[1+\left(\frac{b_1}{a_1}\right)^{0.774}\right]\right\}\right)$$

$$\frac{(1-v)\Delta\sigma_{2p}}{EJ\Delta p} = \frac{\left(b_1/a_1\right)}{1+\left(b_1/a_1\right)} \tag{19}$$

$$+ \left[\frac{\left(b_1/_1\right)}{1+\left(b_1/a_1\right)}\right]\left(1\Big/\left\{1+\left[1.45\left(\frac{h}{2b_1}\right)^{0.9}+0.35\left(\frac{h}{2b_1}\right)^2\right]\left[1+\left(1-\frac{b_1}{a_1}\right)^{1.36}\right]\right\}\right)$$

For calculating the semi-axes of the flood region a_1 and b_1 within the ellipse, the following equations are used:

$$V_{wt} = W_i \big/ (Phie * (1 - S_{or} - S_{Wi})) \tag{20}$$

$$F2 = 2 * V_{wt} \big/ (\pi * h * L_f{}^2) + 0.5 * \sqrt{\left(\frac{4V_{wt}}{\pi * h * L_f{}^2}\right)^2 + 4} \tag{21}$$

$$a_1 = \frac{L_f * \left(\sqrt{F_2} + \frac{1}{\sqrt{F_2}}\right)}{2} \tag{22}$$

$$b_1 = \frac{L_f * \left(\sqrt{F_2} - \frac{1}{\sqrt{F_2}}\right)}{2} \tag{23}$$

160

Where V_{wt} = total volume of the flooded region

F_2 = an intermediate calculation parameter

And all other parameters are the same as those defined in Section 2.2.

165   Pore pressure distribution can be obtained by using equations 24 to 27 (Koning, 1985; Ge & Ghassemi, 2008; Perkins and Gonzalez, 1985):

$$P(\xi, \eta, t) = P_P + \Delta P(\xi) \tag{24}$$

$$\Delta P_1 (\xi) = \frac{q}{2\pi h \lambda_1} ln \left(\frac{3.0\sqrt{\kappa t}}{Lcosh\xi + Lsinh\xi}\right) \xi_1 \leq \xi \leq \xi_2 \tag{25}$$

$$\Delta P_2 (\xi) = \frac{q}{2\pi h \lambda_2} ln \left(\frac{a_1 + b_1}{Lcosh\xi + Lsinh\xi}\right) + \Delta P_1 \xi_0 \leq \xi \leq \xi_1 \tag{26}$$

$$\Delta P_3\,(\xi) = \frac{q}{2\pi h \lambda_3} ln\left(\frac{a_0 + b_0}{Lcosh\xi + Lsinh\xi}\right) + \Delta P_1 + \Delta P_2 \tag{27}$$

$$0 \le \varepsilon \le \varepsilon_0$$

Where ΔP_1 = pore pressure increase at the elliptical boundary of the flood front

$$= \frac{q}{2\pi h \lambda_1} \ln\left(\frac{3.0\sqrt{\kappa t}}{a_1 + b_1}\right)$$

P_p = native pore pressure of the reservoir

ΔP_2 = pore pressure increase between the flood front and the thermal front (compressibility effect is assumed negligible) $= \frac{q}{2\pi h \lambda_2}\ln\left(\frac{a_1 + b_1}{a_0 + b_0}\right)$

$\lambda_1 = {kk_{rw}}/{\mu_0}$, $\lambda_2 = {kk_{rw}}/{\mu_{hot}}$ and $\lambda_3 = {kk_{rw}}/{\mu_{cold}}$ = reservoir, flood region and cool region fluid mobilities, respectively

$K = \frac{k}{Phie\mu_0 c_f}$ = reservoir diffusivity constant

J = linear coefficient of pore pressure expansion $= \frac{1-2v}{E} - \frac{c_{gr}}{3}$

c_{gr}, c_w and c_f = grain, water and formation compressibility, respectively

k = reservoir permeability

k_{rw} = relative permeability to "water" (i.e., injected fracture fluid filatrate) at residual oil saturation

μ_0 = viscosity of oil at reservoir temperature

μ_{hot} = viscosity of fracture fluid filtrate at reservoir temperature

μ_{cold} = viscosity of fracture fluid filtrate at cool temperature

ξ and η = axial parameters for an elliptical coordinate system, as shown in Figure 6.

ξ_0, ξ_1 and ξ_2 = the boundaries of cool region, flood region, and pressure front, respectively

For convenience of analysis and visualization, it is beneficial to use an elliptical coordinate system for this type of analysis. An elliptical coordinate system $(\xi - \eta)$ is shown in Figure 6. Confocal ellipses and hyperbolae create two-dimensional orthogonal elliptical coordinates. Two foci are located at fixed positions of $-L_f$ and L_f on the X-axis of the Cartesian coordinate system (X-Y). For any point around the fracture in an X-Y coordinate, the elliptical coordinate can be set as (Ge & Ghassemi, 2008):

$$X = L_f \cosh\xi \, \cos\eta \tag{28}$$

$$Y = L_f \sinh\xi \, \sin\eta \tag{29}$$
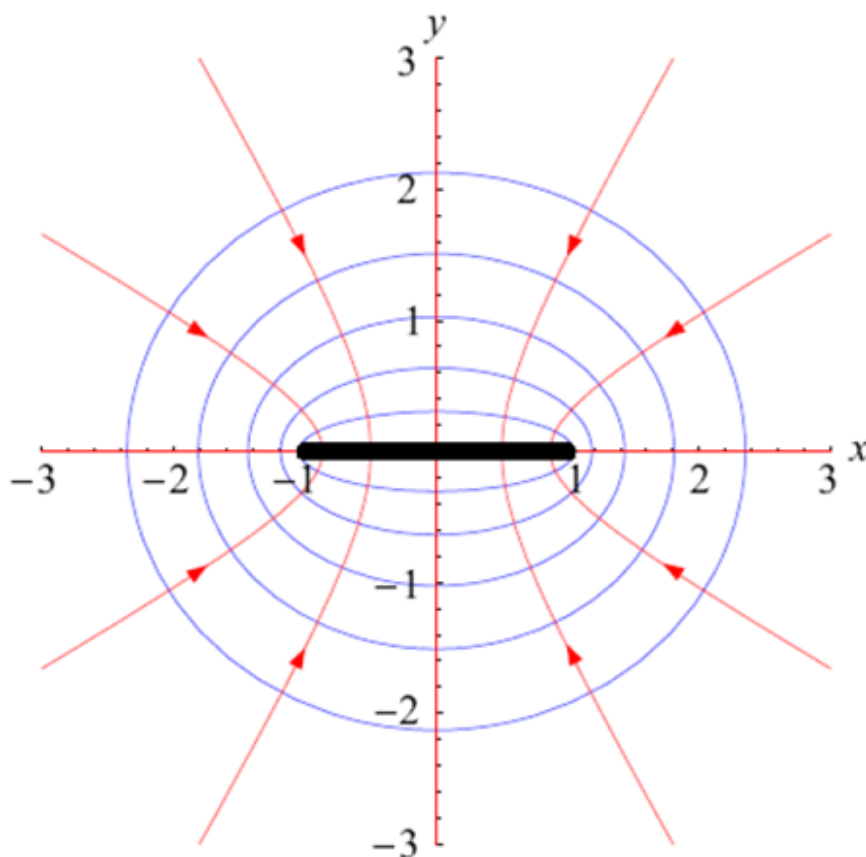
Figure 6: Elliptical coordinate, blue lines are ξ and red lines are η (Ge & Ghassemi, 2008)

2.5 Analysis of Stress Rotation Due to Stress Shadows

The induced stress changes due to stress shadow effects will generally result in principal stresses that are rotated with respect to the in-situ principal stresses. For analyzing stress rotation around a fracture, principal stress magnitudes are calculated using equations 30 and 31.

$$\sigma_1 = \frac{\sigma_X + \sigma_Y}{2} + \sqrt{\left(\frac{\sigma_X - \sigma_Y}{2}\right)^2 + \tau_{XY}{}^2} \tag{30}$$

$$\sigma_3 = \frac{\sigma_X + \sigma_Y}{2} - \sqrt{\left(\frac{\sigma_X - \sigma_Y}{2}\right)^2 + \tau_{XY}{}^2} \tag{31}$$

Where σ_1 and σ_3 = principal stresses in the X-Y plane

σ_X = stress in the X direction = $\sigma_H + \Delta\sigma_X + \Delta\sigma_{2T} + \Delta\sigma_{2p}$

σ_Y = stress in the Y direction = $\sigma_h + \Delta\sigma_Y + \Delta\sigma_{1T} + \Delta\sigma_{1p}$

τ_{XY} = shear stress in the X-Y plane = $\Delta\tau_{XY}$

Principal planes are defined as the planes on which the principal stresses act and the shear stress is zero. Stress rotation angle is determined by using Equation 32.

$$2\theta_P = tan^{-1}\frac{2\tau_{XY}}{\sigma_X - \sigma_Y} \tag{32}$$

Where θ_P = stress rotation angle around the vertical axis.

2.6 Evaluation of Shear Failure Potential on Natural Fractures

The shear failure potential of natural fractures around an induced hydraulic fracture was analyzed in this work, because slip on natural fractures can induce microseismic events which can be detected and located if appropriate monitoring technologies are used. Several failure criteria for shear failure for rock joints have been developed by various scholars including the Barton-Bandis failure criterion (Barton & Choubey, 1977; Barton and Bandis, 1980, Barton, 1976). Various investigators have offered criteria for shear failure of rock mass (Sheorey, 1997) such as the Bieniawski-Yudhbir criterion, the Ramamurthy criterion, and the Hoek-Brown criterion (Hoek & Brown, 1980). In petroleum geomechanics, the Mohr-Coulomb failure criterion is widely used due to its simplicity. The Mohr Coulomb failure criterion for natural fracture is given as follows:

$$|\tau_f| = c + \sigma_n'tan\varphi \tag{33}$$

Where c = cohesion (generally considered zero as a lower bound for strength in microseismic prediction)

σ_n' = effective normal stress

τ_f = shear strength of fracture

ϕ = natural fracture friction angle

225   Failure along the natural fracture can be quantified in terms of a slip criterion which is defined as follows:

$$Slip = |\tau| - |\tau_f| \qquad\qquad (34)$$

Where $Slip$ = slip parameter (values $\geq$ 0 denote slip)

       $\sigma_n{'}$ = effective normal stress

       $|\tau|$ = magnitude of shear stress, acting on natural fracture face

A negative value of the parameters indicates that shear failure is not predicted for the fracture.

230   For analyzing this slip criterion, shear and normal stress on fracture plane are determined by using the following methodology (Zoback, 2007):

   1. Transforming stress from the X-Y-V coordinate to the geographic coordinate (N-E-D) (Figure 7). For this, the stress tensor around the hydraulic fracture in the X-Y-V coordinate system, denoted by S (Equation 35) is transformed to S_g, which denotes stress in the geographic coordinate system (equations 36 and 37)

$$S = \begin{bmatrix} \sigma_V & 0 & 0 \\ 0 & \sigma_X & \tau_{XY} \\ 0 & \tau_{XY} & \sigma_Y \end{bmatrix} \qquad\qquad (35)$$

$$S_g = R_1{'} S\ R_1 \qquad\qquad (36)$$

235   Where

$$R_1 = \begin{bmatrix} cosacosb & sinacosb & -sinb \\ cosa\ sinbsinc - sinacosc & sinasinbsinc + cosacosc & cosbsinc \\ cosasinbcosc + sinasinc & sinasinbcosc - cosasinc & cosbcosc \end{bmatrix} \qquad (37)$$

Because σ_V is vertical:

       a = azimuth of maximum horizontal stress (AZ-σ_H) $-\frac{\pi}{2}$ (radians)

       $b = -\frac{\pi}{2}$ (radians)

       $c = 0$

240   2. Transforming stress from the geographic coordinate (denoted by S_g) to an arbitrary coordinate system (denoted by S_f), which is defined by the orientation of a natural fracture (Equation 38).

$$S_f = R_2\ S_g\ R_2{'} \qquad\qquad (38)$$

Where

$$R_2 = \begin{bmatrix} \cos(str) & \sin(str) & 0 \\ \sin(str)\cos(dip) & -\cos(str)\cos(dip) & -\sin(dip) \\ -\sin(str)\sin(dip) & \cos(str)\sin(dip) & -\cos(dip) \end{bmatrix} \tag{39}$$

245

Str = strike (measure clockwise from north; see Figure 8 for definition of strike using the right-hand rule)

dip = dip angle (measured downwards from the horizontal plane)

Figure 8 shows the natural fracture in three dimensions. If shear failure occurs in the fracture plane the slip direction is denoted by the rake angle (i.e., the angle between the slip direction and a horizontal line contained within the fracture plane).

250 Finding the shear and normal stresses acting on the fracture plane as follows:

$$\tau = S_r\,(3,1) \tag{40}$$

$$\sigma_n = S_f\,(3,3) \tag{41}$$

$$S_r = R_3\,S_f\,R_3{}' \tag{42}$$

$$R_3 = \begin{bmatrix} \cos(rake) & \sin(rake) & 0 \\ -\sin(rake) & \cos(rake) & 0 \\ 0 & 0 & 1 \end{bmatrix} \tag{43}$$

τ (hence potential slip direction) acts in the direction of the rake angle (see Figure 8 for definition), which is determined as follows:

If $S_f(3,2) > 0$ and $S_f(3,1) > 0$ or $S_f(3,2) > 0$ and $S_f(3,1) < 0$; then

$$rake = \arctan\left(\frac{S_f(3,2)}{S_f(3,1)}\right) \tag{44a}$$

255 If $S_f(3,2) < 0$ and $S_f(3,1) > 0$; then

$$rake = \pi - \arctan\left(\frac{S_f(3,2)}{-S_f(3,1)}\right) \tag{44b}$$

If $S_f(3,2) < 0$ and $S_f(3,1) < 0$; then

$$rake = \arctan\left(\frac{-S_f(3,2)}{-S_f(3,1)}\right) - \pi \tag{44c}$$

In this work, the values of σ_V, σ_X, σ_Y and τ_{xy} used as input for slip analysis were calculated based on in-situ stresses plus stress shadow components (as defined following Equation 29). As such, the effects of induced stresses on natural fractures were considered.
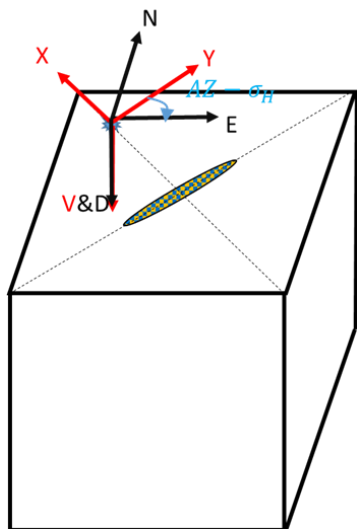
260

Figure 7: Elliptical coordinate, blue lines are ξ and red lines are η (Ge & Ghassemi, 2008)
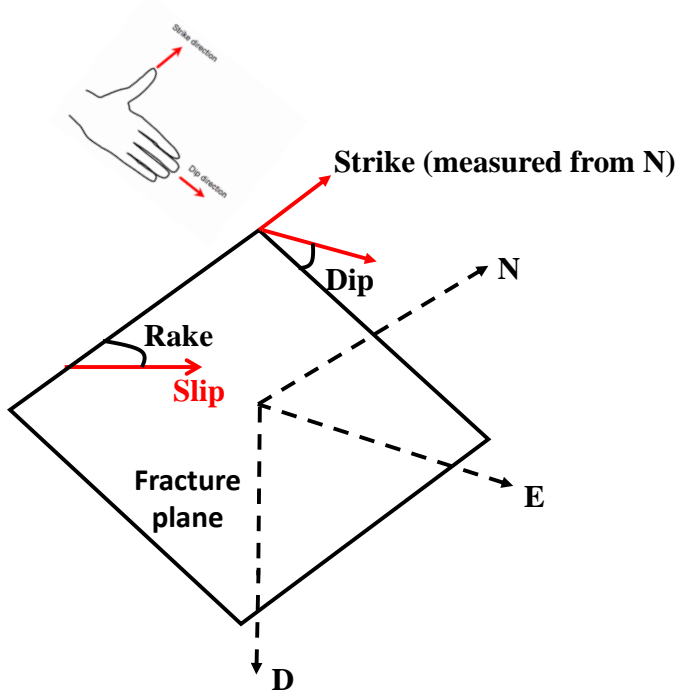
Figure 8: Main orientation attributes of natural fracture (i.e., dip, dip direction and strike), and right hand rule to define strike and dip direction (strike + 90°). Fracture slips in the direction of rake (After Zoback, 2007)

265

3 Case Study Incorporating Stress Shadow Analysis

3.1 Geological Setting

The case study presented in this work is focused on the Bakken Formation in the province of Saskatchewan, in Western Canada.
The Devonian to Carboniferous-age Bakken Formation lies in the subsurface of northeast Montana (U.S.A.), northwest North

270   Dakota (U.S.A.), southeast Saskatchewan (Canada) and southwest Manitoba (Canada) (see Figure 9). This formation hosts
one of the most active oil plays in North America in recent decades. The Bakken Formation is subdivided into the lower,
middle and upper members (Angulo & Buatois, 2012; Gorjian, 2019) (Figure 10). The lower and upper members are organic-
rich shales, which were deposited under oxygen-depleted conditions in a shelf environment. The calcareous to dolomitic sandy
to silty middle member was deposited in a shallow marine environment (Halabura et al., 2007; Gorjian, 2019) and has been

275   subdivided informally by many authors (Lefever et al., 1991; Gorjian, 2019). The middle member serves as the oil reservoir;
multi-stage hydraulic fracturing is generally required to achieve economic production rates from this member.
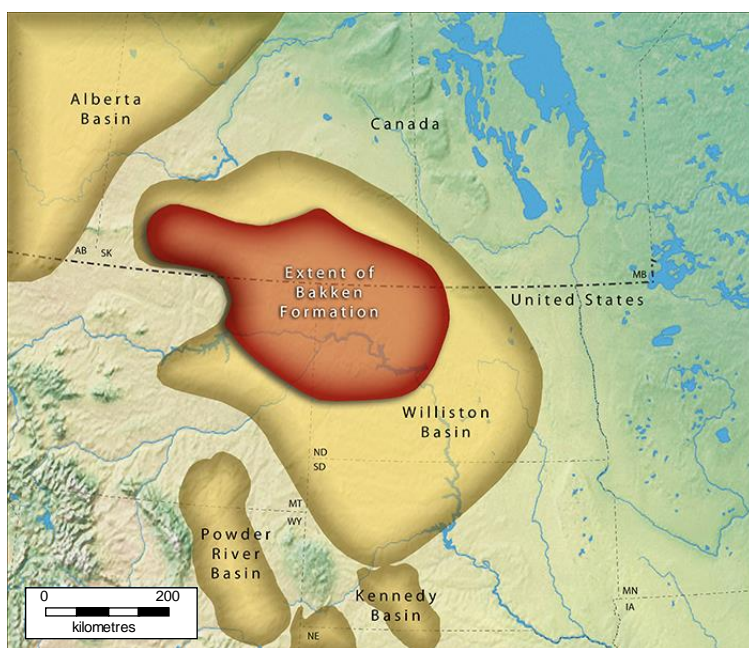
**Figure 9: Figure 9: Map showing the extents of the Bakken Formation within the Williston Basin, northwestern North America.
(After EERC, 2014)**

280   The authors previously completed an extensive study of the Bakken Formation in the Viewfield region of southeast
Saskatchewan, including geomechanical site characterization using data from 13 wells, numerical simulation of hydraulic
fracture simulation using GOHFER, and comparison of the simulation results to field data. Interested readers are referred to
Gorjian (2019) for details. In this paper, we focus on stress shadow analyses conducted on one well from the original study,
referred to here as well S for simplicity (the actual well name is 191/14-15-007-07w2). Well S was chosen because of the

285 availability of instantaneous shut-in pressures (ISIP's) from each stage of a multi-stage hydraulic fracture treatment, and its

proximity to another well (11/16-28-008-07w2) which had been used for rock mechanical properties analysis.
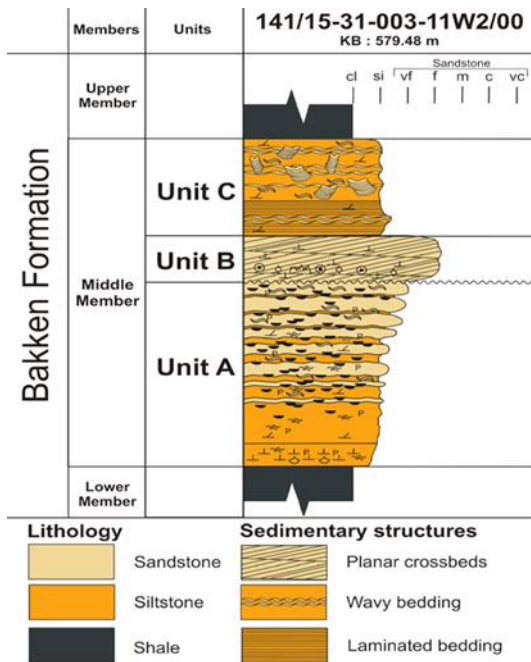
Figure 10: Figure YY. Stratigraphic chart showing a typical geological section of the Bakken Formation in Saskatchewan (National
290 **Energy Board, 2015)**

Well S was completed by 30[1]-stages of hydraulic fracturing. Each stage used 4 tonnes of proppant mixed with 32.9 m^3 of ELE-Stim for proppant stages and ELE-Stim 18cp for non-proppant stages fracture fluid injected over a time interval of 47 minutes. For initial conditions (i.e., no stress shadow effects; key input parameters as summarized in Table 1), the numerical simulator predicted a maximum fracture height of 19.8 m, half-length of 81 m, and average propped width of 5.7 mm.

295 **Table 1: Average properties assigned for Middle-Bakken reservoir interval as initial condition**

Parameter	Minimum Horizontal Stress Magnitude (Mpa)	Maximum Horizontal Stress Magnitude (Mpa)	Vertical Stress Magnitude (Mpa)	Reservoir Pressure (Mpa)	Young's Modulus (Gpa)	Poisson's Ratio	Porosity (%)	Permeability (md)	Biot's Coefficient
Average Value	20.8	26.1	35	13.7	25	0.25	11	0.11	0.8

---

[1] The first stage of this fracture treatment failed, so the first successful stage is titled stage 2.

3.2 Stress Shadow Modeling for a Single Stage Fracturing

300 **3.2.1 Mechanical Stress Shadow**

Figures 12 and 13 were generated by the author using Matlab code written to solve the equations presented in sections 2.1 and 2.4. Figure 11 shows the normal stresses perpendicular and parallel to the fracture at the end of treatment (immediately after shut-in), whereas Figure 12 shows the shear stress in the horizontal plane and the rotation angle of the principal stresses. According to these results, if hydraulic fracturing of stage 3 began immediately after shut-in of stage 2, the minimum horizontal

305 stress would be greater than the original in-situ value (22.7 MPa compared to 20.8 MPa), the maximum horizontal stress would be less than the original value (25.9 MPa compared to 26.1 MPa), and the tips of the hydraulic fracture would be rotated 11° towards stage 2 (rather than parallel to the stage 1 fracture).

In general, it is most important to note that the stress shadow results in an increase in minimum horizontal stress, hence an increase in the pressure required to initiate and propagate a fracture, and in the tendency for the induced fracture to deviate

310 towards the previous fracture stage. Furthermore, sensitivity analyses showed that these effects become more pronounced as fracture stage spacing is decreased, and the fracture rotation tendency can become particularly pronounced if the anisotropy in horizontal stresses is small. One final note pertaining to the results shown here is that these results represent an upper bound because they were generated for a scenario with no lag time between stages 2 and 3. In reality, pressure dissipation will occur with time following stage 2, which would diminish the magnitude of the stress shadow. Eventually, the fracture width would

315 become constant with time, once both faces are in firm contact with proppant.

3.2.2 Thermo and Poro-elastic Stress Shadows

Thermo and poro-elastic stress shadows were analyzed by writing code in Matlab to solve the equations presented in sections 2.2 and 2.3. It should be noted that all the key input parameters in this analysis is given in Table A.1. To the best of authors' knowledge, it is the first time that the thermal properties (Thermal conductivity, linear coefficient of thermal expansion,

320 specific heat of mineral grains per unit volume) for Bakken Formation are measured in laboratory and reported. These shadows were found to be insignificant for the Bakken Formation, largely due to its low permeability (hence the limited extent of pressure increase and cooling around fractures). To illustrate the use of these solutions, extreme cases were analyzed; the results are given in Appendix A (thermo-elastic) and Appendix B (poro-elastic). It is worth noting that it is not necessary to analyze the distribution of poro- and thermo-elastic stress shadows throughout the entire model domain, if seeking to minimize

325 analytical effort while assessing the relative significance of the different stress shadow mechanisms. Rather, it would be sufficient to calculate the change in minimum horizontal stress at a point corresponding to $\theta = 90°$ and R = fracture stage spacing for each stress shadow mechanism (see Figure 4). Any stress change deemed negligible at this point should have a negligible influence on a fracture being initiated at this point. For example, in the case analyzed here, the horizontal stress change predicted at this point is 1.9 MPa for the mechanical stress shadow mechanism, 0 MPa for the thermo-elastic and 0 for

330 the poro-elastic.

3.2.3. Stress Shadow Modeling for Multistage Hydraulic Fracturing

The lateral spacing and time lag between successive stages for well S are shown in figures 13 and 14, respectively.

3.2.3.1 Stress Shadow of Stage 2 on Stage 3

In Section 3.2.1, the stress shadow effect for stage 3 was analyzed for conditions existing immediately after shut-in for stage 335 2. However, in practice there is generally a time lag between performing the successive fracture stages, which should be considered because during that time fluid can leak off from the fracture to the formation, thus decreasing pressure and the magnitude of the stress shadow effect. Based on a 73 minute time lag between stages 2 and 3 (see Figure 14), the calculated distributions of normal stresses are shown in Figure 15 and shear stresses and principal stress rotation in XY plane are shown in Figure 16.

340

(a)   (b)

Legend

Horizontal well	⎯⎯⎯
Hydraulic fracture for stage #2 and #3 (Viewed from above)	┊
Original value for in-situ stress	⎯
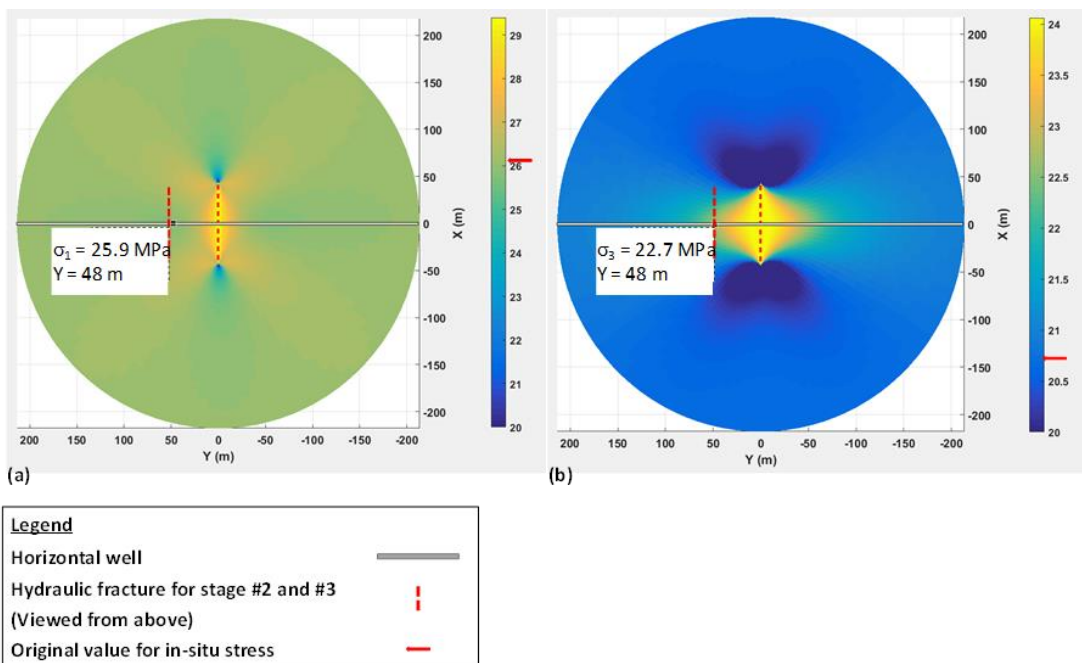
Figure 11: Predicted stress distribution resulting from mechanical stress shadow effects (immediately after shut-in) around a single hydraulic fracture, viewed from above (plan view). (a) Normal stress in the direction of X-axis; (b) normal stress in the direction of
345 **Y-axis. The Y-axis is aligned parallel to the in-situ minimum horizontal stress. The vertical dashed line at the centre shows the location of the newly created fracture (stage 2); the vertical dashed line offset 48 m to the left represents the location planned for the next fracture (stage 3).**

(a)   (b)

Legend	
Horizontal well	
Hydraulic fracture for stage # 2	⁞
Hydraulic fracture for stage #3	⋮
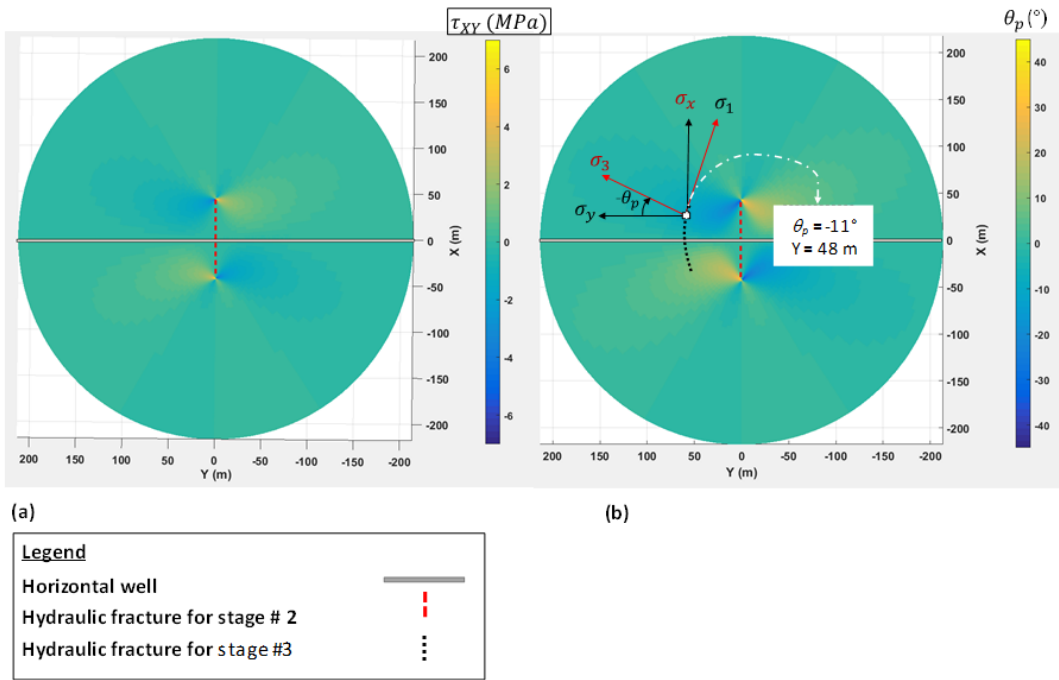
350 **Figure 12: Predicted stress distribution resulting from mechanical stress shadow effects (immediately after shut-in) around a single hydraulic fracture, viewed from above (plan view). (a) Induced shear stress in the XY plane; and (b) principal stress rotation angle.**
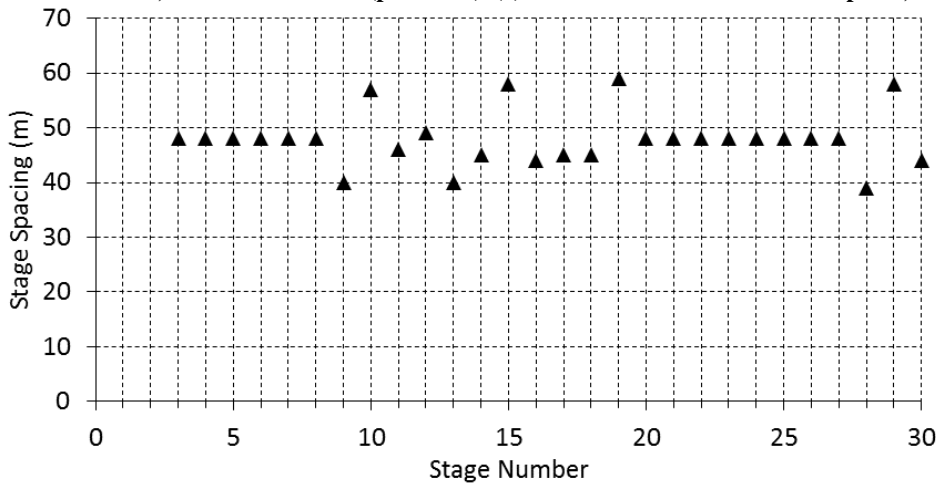
Figure 13: Stage spacing in well S. The spacing plotted represents the distance between the stage represented on the X-axis and the preceding stage. For example, the value of 48 m plotted for stage 3 indicated a 48 m spacing between stage 2 and stage 3. (Note:
355 **Stage 1 in this treatment program failed).**
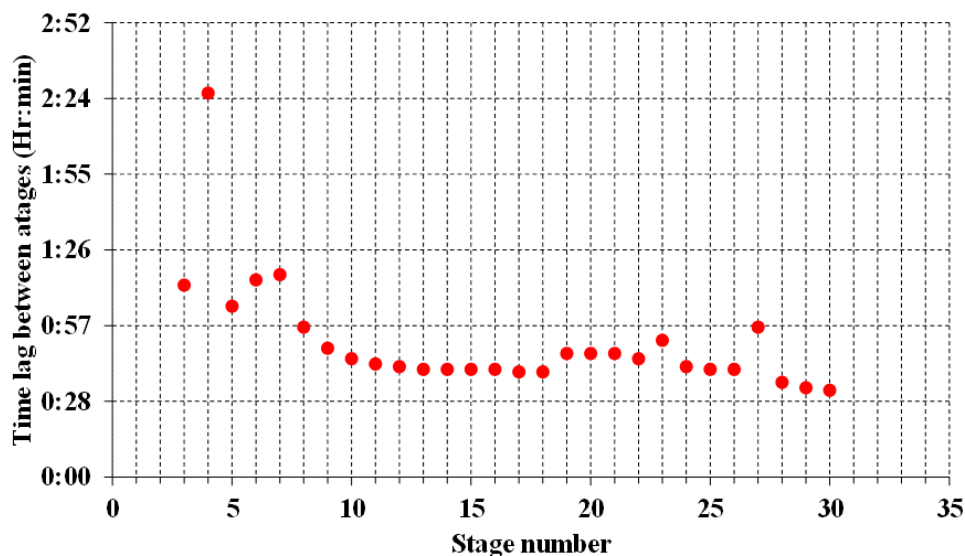
Figure 14: Inter-stage time lags recorded for well S. The time lag plotted represents the time elapsed between start of injection for the stage represented on the X-axis and shut-in of the preceding stage. (Note: Stage 1 in this treatment program failed.)

360
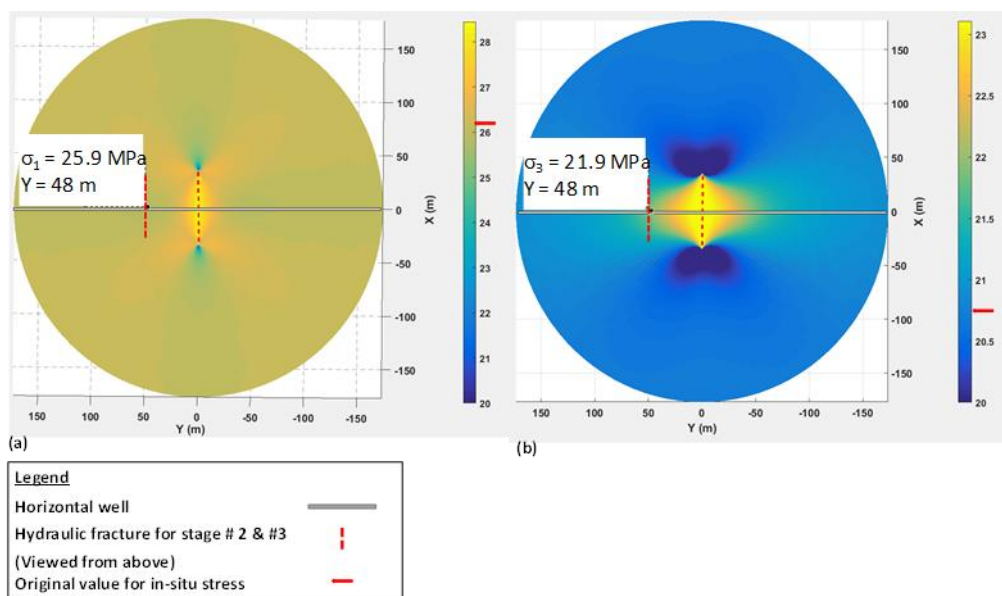
Figure 15: Predicted stress distribution resulting from mechanical stress shadow effects (73 minutes after shut-in) around a single hydraulic fracture, viewed from above (plan view). (a) Normal stress in the direction of the X-axis; (b) normal stress in the direction of the Y-axis. The Y-axis is aligned parallel to the in-situ minimum horizontal stress. The vertical dashed line at the centre shows the location of the newly created fracture (stage 2); the vertical dashed line offset 48 m to the left represents the location planned for

365 **the next fracture (stage 3).**

(a)   (b)

Legend	
Horizontal well	———
Hydraulic fracture for stage # 2	
Hydraulic fracture for stage #3	

Figure 16: Predicted stress distribution resulting from mechanical stress shadow effects (73 minutes after shut-in) around a single hydraulic fracture, viewed from above (plan view). (a) Induced shear stress in the XY plane; and (b) principal stress rotation angle

Figure 17 shows the minimum horizontal stress (σ_Y at X=0), maximum horizontal stress (σ_X at X=0) and vertical stress versus Y at X=0 (center of fracture) around the hydraulic fracture at stage 2 both immediately after shut-in and 73 minutes after shut-in. General observations based on Figure 17 are as follows:

- Based on defining the stress shadow zone as the zone in which a stress change of 0.5 MPa has occurred, the vertical lines #h0 (Y = 122m) and #ht (Y = 82m) show the boundaries of the stress shadow zone for scenarios of 0 and 73 minutes of time lag, respectively. This suggests that the stage spacing required to avoid stress shadow effects for hydraulic fracturing of stage 3 would be 122 m and 82 m, for a time lag scenarios of 0 and 73 minutes, respectively.

- The maximum horizontal stress decreases more acutely than minimum horizontal stress. This is shown with the stress shadow zone (as shown by dashed line #H0) at Y = 38 m for immediately after stage 2 and at Y = 25 m (as shown by dashed line #Ht) for a time lag of 73 minutes.

- The vertical stress has the same trend as maximum horizontal stress and can be assumed unchanged for any distance further than 38 m.
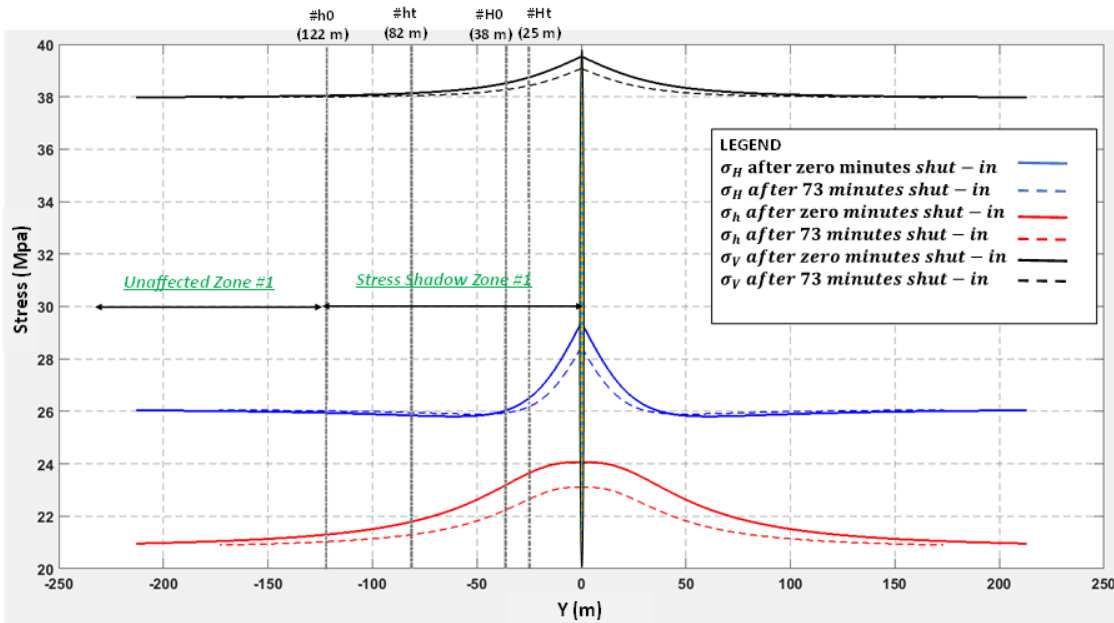
Figure 17: Horizontal stresses in the X direction (parallel to the fracture), Y direction (perpendicular to the fracture) and vertical direction versus Y at X = 0 around a hydraulic fracture at stage 2 after shut-in times of zero and 73 minutes. The dashed lines #h0, #ht denote the limits of the stress shadow zones for the minimum horizontal stress after 0 and 73 minutes of shut-in, and the dashed lines #H0, #Ht denote the limits of the stress shadow zones for the maximum horizontal stress and vertical stress after 0 and 73 minutes of shut-in. The limits of the vertical stress shadow zone are not shown, but they are effectively the same as the maximum horizontal stress shadow zone. [Note: The criterion used to delimit stress shadow zones in this work is a change of 0.5 MPa]

3.2.3.2 Cumulative Stress Shadow of Effects of Stage 2 and 3 on Stage 4

By considering 219 minutes and 146 minutes lag times after stages 2 and 3 respectively, the predicted distribution of minimum horizontal stress and principal stress rotation angle at Y = 96 m (i.e., the location of stage 4) are shown in Figure 18. Figure 19 shows the minimum horizontal stress and maximum horizontal stress versus Y at X=0 (center of fracture). Notable observations based on Figures 18 and 19 are as follows:

- Predicted minimum horizontal stress at Y = 96 m (stage 4) is 22.7 MPa, compared to 20.8 MPa initially. [Note: Model validation by comparison of model predictions against field data is shown in discussion section.]

- There is a predicted region of stress reversal at approximately Y = 25 m.

- To avoid stress shadow effects, stage 4 would have to be spaced 152 m from stage 3 (i.e., nearly 200 m from stage 2) based on a shadow threshold criterion of 0.5 MPa.

- The predicted principal stress rotation angle doubles from 6° to 12° when accounting for a cumulative stress shadow on stage 4 caused by stages 2 and 3.
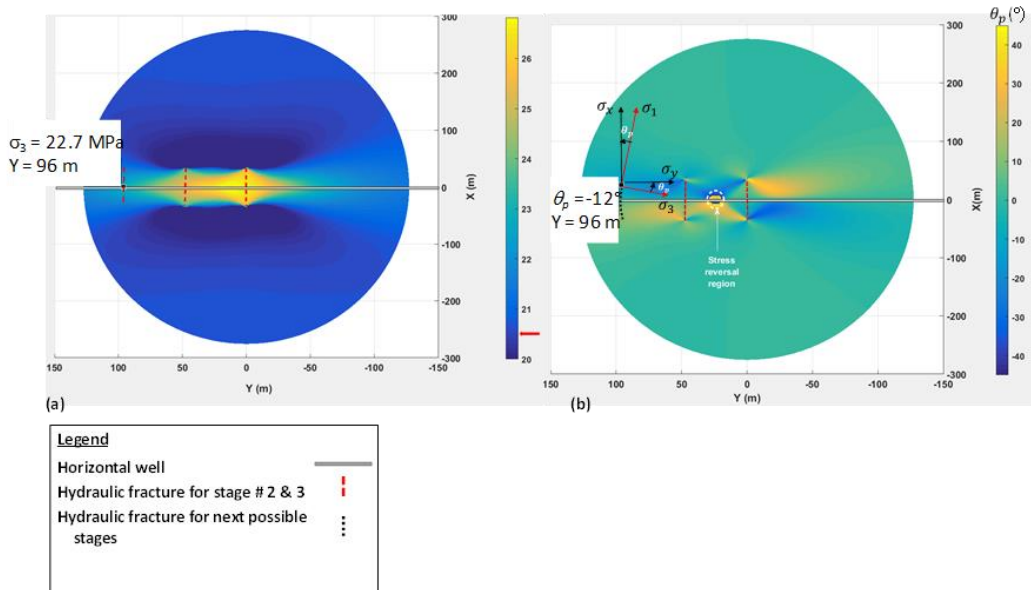
Figure 18: Predicted stress distribution resulting from cumulative mechanical stress shadow effects resulting from stage 2 and 3, at the time when pumping begins for stage 4. (a) Induced shear stress in the XY plane; and (b) principal stress rotation angle.
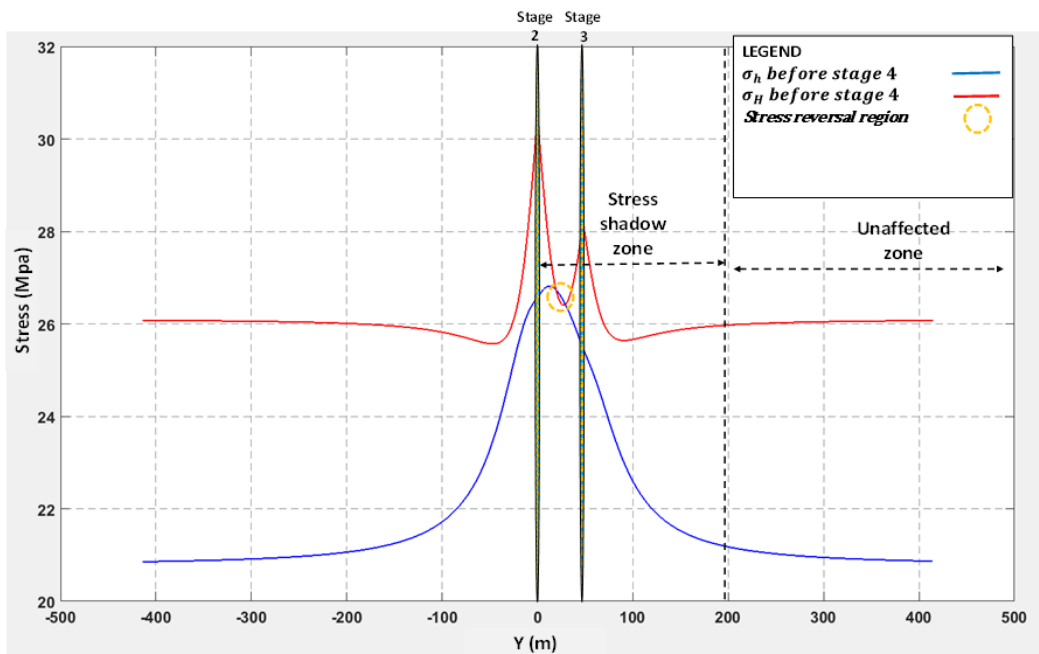
Figure 19: Minimum horizontal stress and maximum horizontal stress vs. Y at X=0 due to hydraulic fracturing of stages 2 and 3 at the beginning of pumping for stage 4.

3.2.3.3   Stress Shadow for the Final Fracture Stage ("Stage 30")

Calculations for stage 30 were undertaken in a manner consistent with those described for stage 4, except in this case the time lag and distance between stage 2 and 30 were used to calculate stage 2's stress shadow for stage 30. Then the time lag and

410   distance between stages 3 and 30 were used to calculate stage 3's stress shadow for stage 30, and so on (up to stage 29). Upon summing the stress changes resulting from stage 2 through 29, the stress conditions during stage 30 were obtained.

Figure 20 shows the predicted minimum horizontal stress magnitude during stage 30. At X = 0 m and Y = 1341 m (center of stage 30 fracture), the minimum horizontal stress was calculated as 25.4 MPa (compared to 20.8 MPa originally). The principal stress rotation angle is shown in Figure 21. This figure shows a rotation angle of 35° at the tip of the fracture, which is greater

415   than the 6° predicted for the effect of stage 2 on stage 3 (Figure 16). Figure 22 shows horizontal stress magnitudes in the X and the Y directions versus Y at X = 0 (center of fracture) immediately before stage 30. This figure also reveals that the vertical line at Y = 1294 m is the boundary of a stress reversal zone. Beyond this boundary (i.e., for Y > 1294 m), the horizontal stress state become nearly isotropic up to Y = 1341 m, beyond which normal stress in the X direction becomes greater than normal stress in the Y direction. This result is important because it suggests that fracture orientation could rotate by up to 90°, or there

420   might not be a strongly preferred growth direction at all.
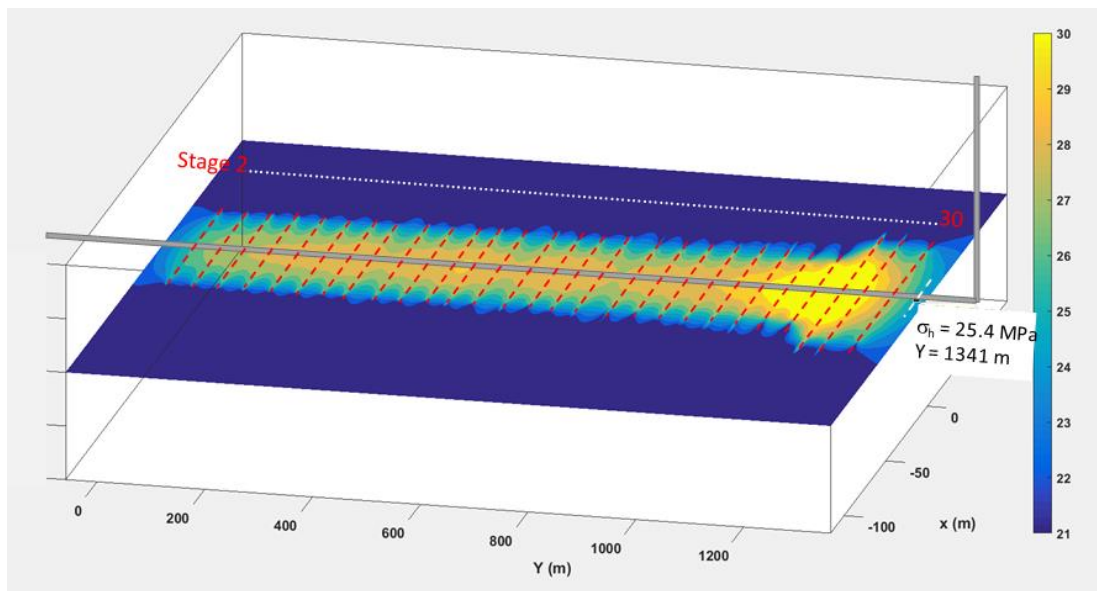
Figure 20: Predicted minimum horizontal stress (MPa) at the time of stage 30 (at Y = 1341 m, which is shown by the white dashed line)
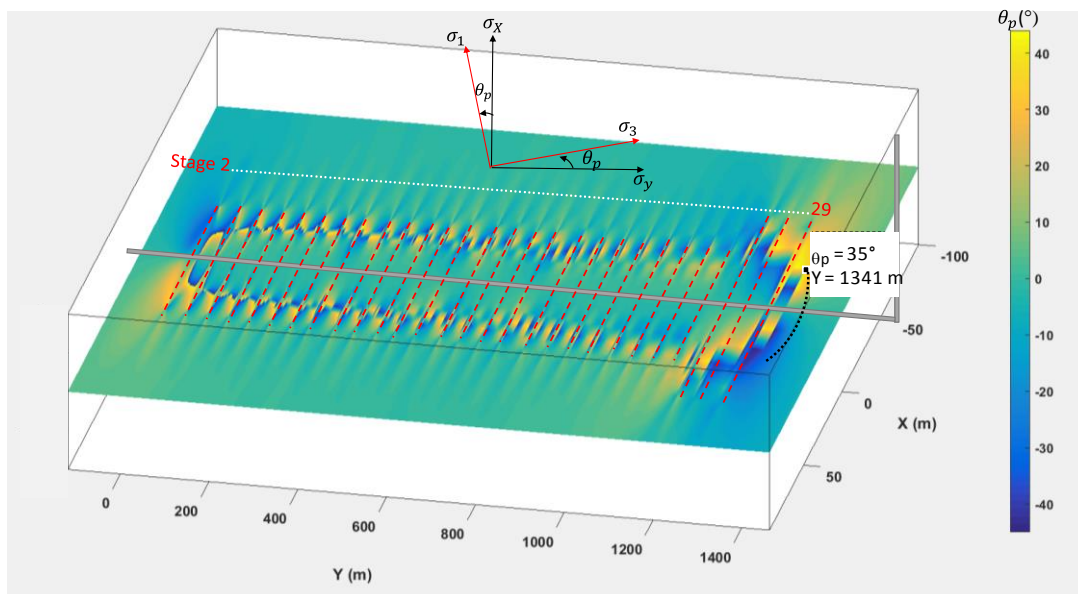
Figure 21: Rotation angle of principal stress due to the combined effects of all stages before stage 30 (at Y=1341 m), showed by black dashed line.
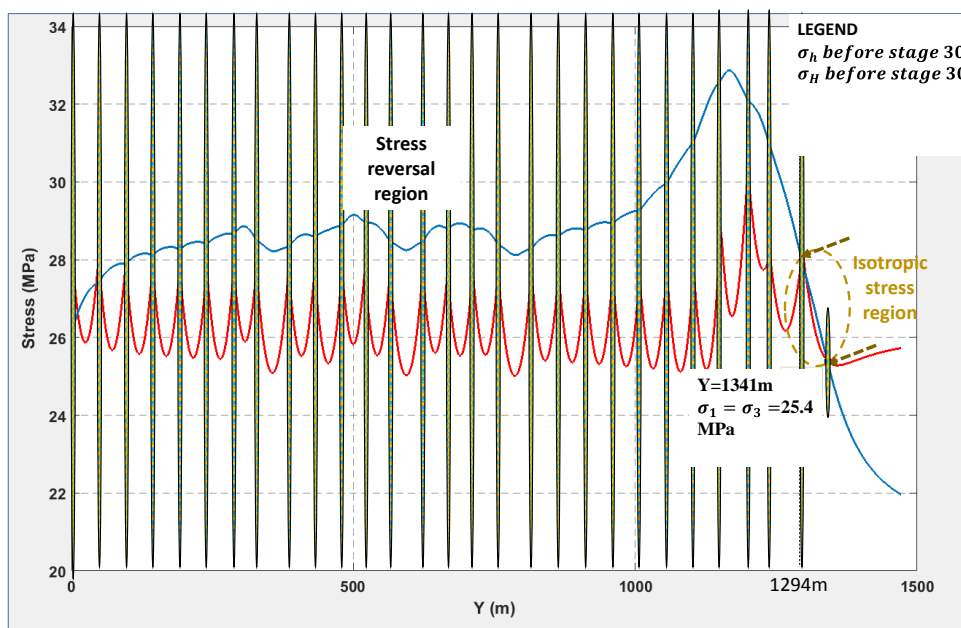
Figure 22: Horizontal stresses in the X and Y directions at the time of stage 30, showing the cumulative stress shadow resulting from stages 2 to 29.

3.2.3.4 Model Simplification

Given that the stress changes occurring along the well trajectory (at each fracture port) are the only components of stress change that can be used as input to Gohfer, calculation of the full stress field is not useful for fracture simulations. For such conditions, the following simplified equations can be used for stress shadow modeling. For $X = 0$ (for any point along the well trajectory), the stress shadow in the Y and X directions for stage n can be calculated by simplifying equations 1 and 2 as follows:

$$\Delta\sigma_{Y,X=0} = \sum_{i=i_i}^{n-1} -\frac{2E\varpi_i}{(1-v^2)\pi h_{fi}}\left[\frac{Y_i}{\left(Y_i^2 + \frac{L_i^2}{4}\right)^{\frac{1}{2}}} - 1 + \frac{Y_i L_i^2}{4 * \left(Y_i^2 + \frac{L_i^2}{4}\right)^{\frac{3}{2}}}\right] \tag{45}$$

$$\Delta\sigma_{X,X=0} = \sum_{i=i_i}^{n-1} -\frac{2E\varpi_i}{(1-v^2)\pi h_{fi}}\left[\frac{Y_i}{\left(Y_i^2 + \frac{L_i^2}{4}\right)^{\frac{1}{2}}} - 1 - \frac{Y_i L_i^2}{4 * \left(Y_i^2 + \frac{L_i^2}{4}\right)^{\frac{3}{2}}}\right] \tag{46}$$

Where: i_i = the first fracture stage

E and v = Young's modulus and Poisson's ratio (statics values)

h_{fi}, L and ϖ_i = fracture height, length and average propped width

Y_i = the spacing between stage i and stage n

Given that horizontal stresses may be reversed within the stress reversal region, the minimum horizontal stress must be assessed as follows:

$$\sigma_3 = \min[(\sigma_X + \Delta\sigma_X), (\sigma_Y + \Delta\sigma_Y)] \tag{47}$$

The model may be further simplified by assuming constant values for fracture length (L_i), average width (ϖ_i) and fracture height (h_i) by assuming the propped values for these parameters (i.e., rather than modeling leakoff for each stage, taking the final values for these parameters after pressures have dissipated and the fracture dimensions are controlled solely by the proppant contained within the fractures). Results obtained using this simplified approach seem promising, as illustrated in Figure 23. This figure suggests that the results obtained using the simplified model compare favourably with the more rigorous model, with the discrepancy being less than 0.5 MPa in most cases.
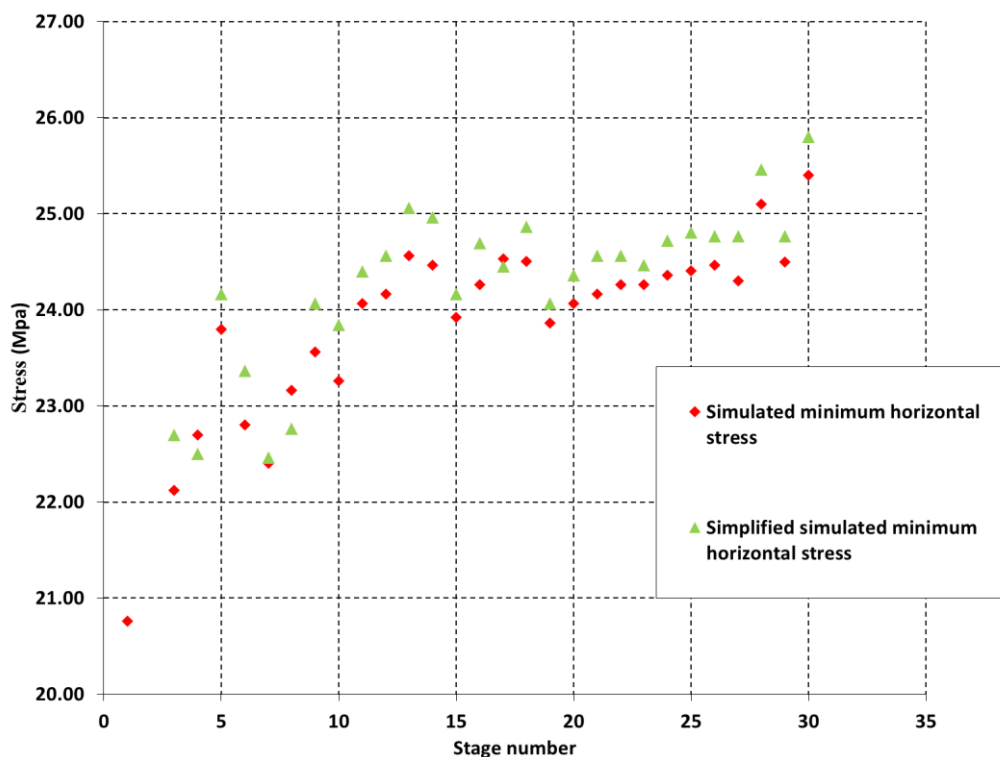
Figure 23: Comparison of simulated minimum horizontal stress (stress shadow effect) calculated with the simplified model (Equation 4.1) and the comprehensive model (see Section 3.4.1).

4   Natural Fracture Shear Failure analysis

455   Hydraulic fracturing operations can be significantly affected by the presence of natural fractures in the reservoir, depending on fracture attributes such as spacing, orientation and shear strength. For example, if natural fractures are present and have properties that make them amenable to shear failure ("slip") during the injection of fracture fluid, dilation of these fractures may result in a zone of increased permeability (i.e., a stimulated zone). Furthermore, slip on natural fractures will generally result in the release of acoustic energy (microseismic events), which means there is a close association between the

460   interpretation of microseismic monitoring data and natural fracture attributes (e.g., Zoback, 2007).

In the stress shadow analysis presented in Section 3, the effects of possible natural fractures were not considered. According to core logging conducted by the authors, natural fractures were observed in one well in the study area, possessing a strike of 155° and dip of 65° (Gorjian, 2019).

Figure 24 shows the results obtained when shear failure was analyzed for scenarios of 115°, 135°, and 155° strike direction,

465   in all cases with a 65° for dip angle. The areas shaded in dark brown on Figure 24 denote areas where natural fracture slip is predicted. It is important to note that this figure shows the regions of natural fracture slip that exists once the hydraulic fracture

shown has reached its full length. It is expected that the shear failure zone would have started near the well and grown progressively outwards as the hydraulic fracture propagated, hence resulting in a zone of slip (and associated microseismic events) extending from the well towards an outer bound delineated by the darkly shaded regions in Figure 24.
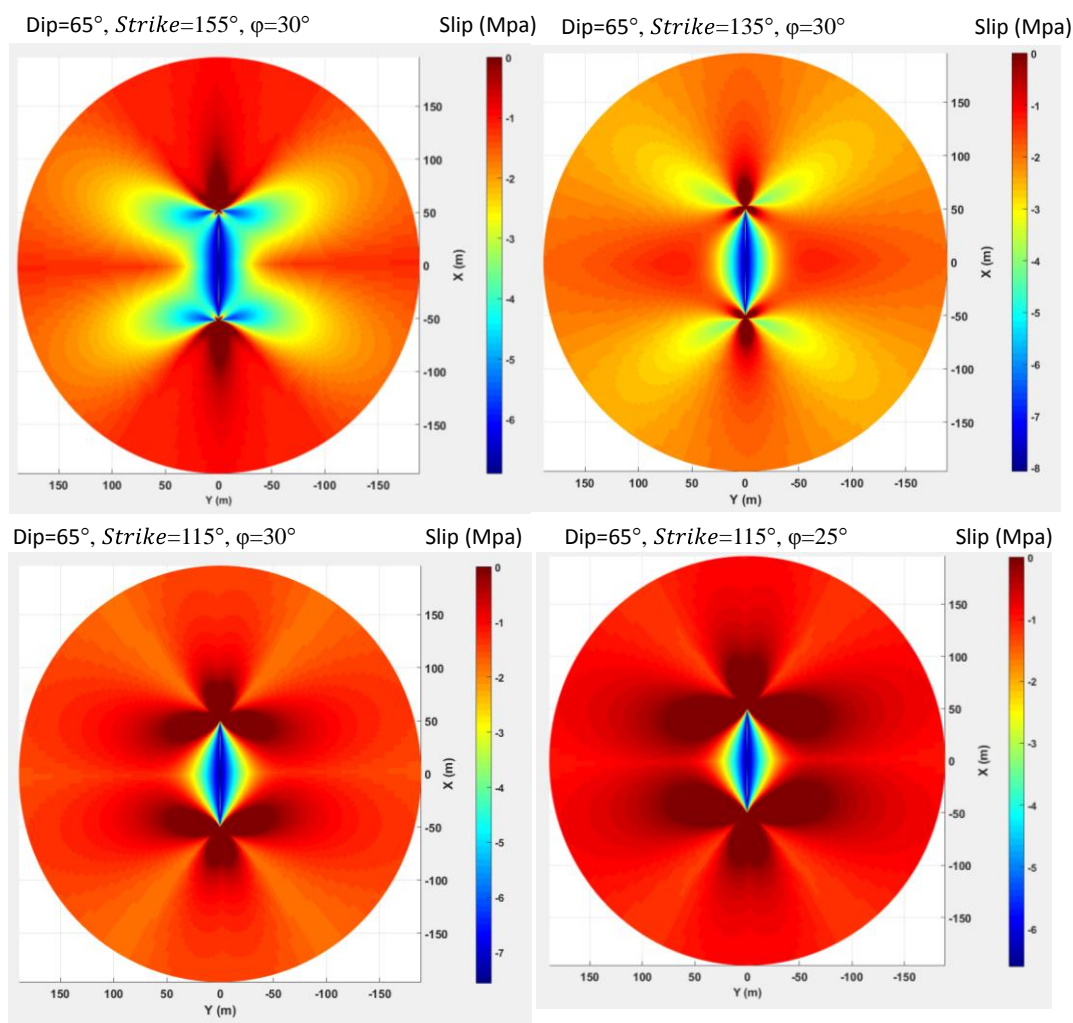
470

Figure 24: Shear failure analysis for natural fractures (hence possible microseismic events showed by dark brown coloured area) with dip angle of 65°, strikes of 115°, 135°, 155° and friction angle of 30° around a hydraulic fracture in the Bakken Formation under conditions representative of well S. For a scenario with strike of 115°, a reduced friction angle of 25° was also analyzed.

475

5 Discussion

5.1 Assessment of Stress Shadow Effect Based on Field Data

To assess the validity of the stress shadow modeling workflow developed in this research (see Section 3.1.2), the instantaneous
480   shut-in pressure (ISIP) values measured for stages 2 through 30 during field operations at well S were plotted and compared
against the model-predicted values of the minimum horizontal in-situ stress (Figure 25). Bottomhole ISIP may be regarded as
an estimate of minimum in-situ stress measurement, especially in fracture treatments involving relatively small, planar
fractures. The predicted trend of increasing minimum horizontal stress with increasing stage number (Figure 25) compares
favourably to the increase in ISIP observed during the treatment program. Both datasets suggest an increase in minimum
485   horizontal stress of approximately 5 MPa, with minor deviations from the trend which may be explainable in part by the
deviations in stage spacing and the time lag between stages.

Even the simplified model results (Equation 45) compare favourably to the field ISIP's. This suggests that the approach is
capable of the predicting minimum horizontal stress (or stress shadow) at each stage (for the Bakken Formation, at least). This
approach can thus be used for modifying stage spacing and/or inter-stage time lag in the Bakken Formation, if shadow-induced
490   stress increases are deemed to adversely affect the effectiveness of hydraulic fracturing operations.
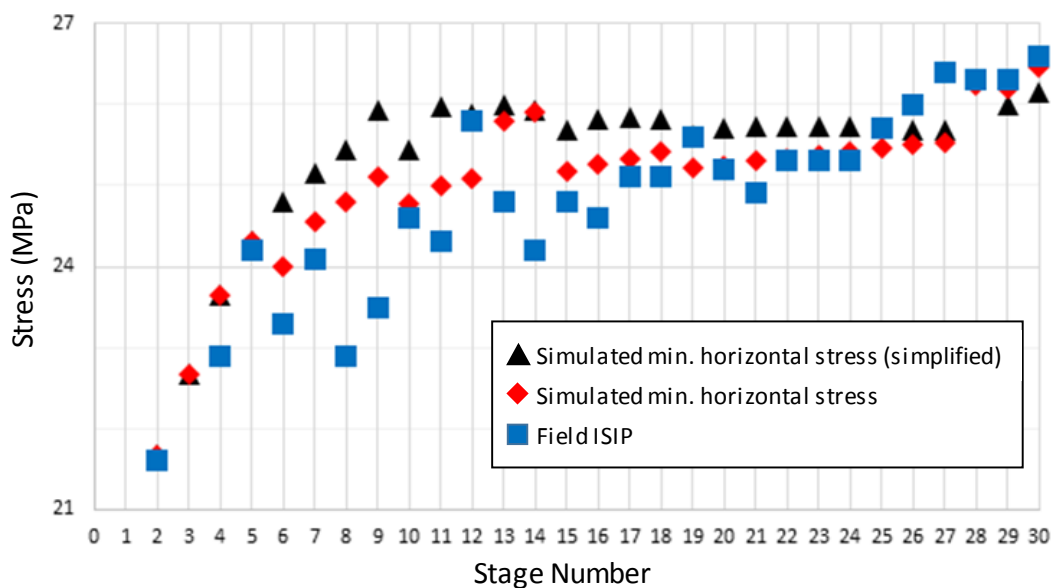
Figure 25: Comparison of simulated minimum horizontal stress and simplified simulated minimum horizontal stress with instantaneous shut-in pressure (ISIP) measurements taken during the stimulation program for well S.

495

5.2 Microseismic Event Evaluation

To evaluate potential hydraulic fracturing-induced microseismic events in the Bakken Formation, shear failure analysis was conducted for an assumed (hypothetical) natural fractures surrounding a hydraulic fracture in the Bakken Formation for conditions existing at well L (191/05-16-009-10w2), which was the only well for which microseismic monitoring data were
500   publically available. Mechanical stress shadow modeling (for a single fracture stage) was repeated for well L, in the same manner as presented for well S in section 3.2.1. Similarly, slip analysis for well L was repeated, in the same manner as presented for well S in section 4. Given the similarity in conditions at wells S and L, and for the sake of brevity, the results are not presented here. Readers may refer to Gorjian (2019) for more details regarding well L.

Table 2 shows a comparison of horizontal extents of shear failure zones with zones of microseismic events logged at well L
505   (see Appendix C). The extents of the predicted zones of shear failure compare favourably with the field data for the scenario with natural fractures striking at 115° with a dip of 65° and friction angles in the range of 25° to 30°. This dip is consistent with observations reported in the lone well that was logged and found to have natural fractures, however the strike is 40° less than the value of 155° that was measured. Given that the strike direction of 155° is based on a limited dataset observed at a different location, it is not unreasonable to expect that fractures striking at 115° might be present near well L. Clearly, more
510   investigation into natural fracture attributes in the Bakken Formation and more public reporting of microseismic monitoring results is required before more confident analyses can be undertaken. When additional data are acquired, the modeling workflow presented here will serve as an effective tool for predicting estimates of the shear failure zone (hence the stimulated reservoir volume).

515   **Table 2: Comparison of the lateral extents of the zones of microseismic activity monitored at well L (Figure C-1) against the predicted extents of shear failure zones for various scenarios of natural fracture orientation.**

Source / Scenario	Length in direction of σ_h (m)	Length in direction of σ_H (m)
Field microseismic data (Appendix C)	190	170
Strike 155°; Dip 65° SW; friction angle = 30° (Orientation observed in well G)	40	200
Strike 135°; Dip 65° SW; friction angle = 30°	20	150
Strike 115°; Dip 65° SW; friction angle = 30°	115	170
Strike 115°; Dip 65° SW; friction angle = 25° (Best match to field data)	165	190

6 Conclusion

520

The following is a list of conclusions based on this study:

- A new toolbox, based on analytical solutions, was developed for predicting stress shadow effects in multi-stage hydraulic fracture, and was demonstrated to compare favourably against ISIP data collected from a well in the study area. The formulation used in this work only considered mechanical stress shadow effects, as thermo and poro-elastic

525
stress shadows were found to be negligible in the Bakken Formation due to the small injection volumes and times and low permeability. However, if the permeability was 2.5 md instead of 0.1 md, the poro-elastic stress shadow should be considered as well. Thermal stress shadow at the tip of fracture can increase the length of fracture; however, it can also decrease the length of fracture if it creates secondary thermo-elastic fractures perpendicular to the primary hydraulic fracture. Analysis showed that the thermo-elastic stress shadow was still too low to create secondary thermal

530
fractures. The effect of thermo-elastic stress shadow at the fracture tip was not analyzed in this work.

- Shear failure of natural fractures around a hydraulic fracture was analyzed and compared against microseismic monitoring data reported for one well in the study area. The results showed a favourable comparison for a scenario with natural fractures striking at 115° with a dip of 65° and friction angles in the 25° to 30° range. More investigation of natural fracture attributes in the Bakken Formation is required in order to implement this type of analysis in the

535
future, in order to predict stimulated reservoir volumes.

Conflict of interest

The authors know of no conflicts of interest with this publication.

Acknowledgements

The authors are grateful to Ridgeback Resources Inc. for partial financial support of this research, and the University of

540
Saskatchewan (College of Graduate and Postdoctoral Studies) for scholarship funding in support of the lead author.

Data Availability Statement

The data that support the findings of this study are available from the corresponding author upon request.

545

References

Barton N, Bandis S. Technical Note: Some Effects of Scale on the Shear Strength of Joints. International Journal of Rock Mechanics and Mining Sciences. 17:69-73, 1980.

Barton N.. The shear strength of rock and rock joints. *Int. J. Rock Mech. Min. Sci. & Geomech. Abstr.,* 13: 255-279, 1976.

550   Boussinesq, M. J.. Application des potentiels a l'etude de l'equilibre et du mouvement des solides elastiques, principalement au calcul des deFormations et des pressions que produisent, dans ces solides, des efforts quelconques exerces sur une petite partie de leur surface ou de leur interieur: Memoire suivi de notes etendues sur divers points de physique mathematique et d'analyse," GauthierVillars, Paris, 722 p, 1885.

Energy & Environmental Research Center (EERC).. Beyond the boom, next generation science and engineering to optimize
555   the Bakken petroleum system, completion technology, 2014. https://www.undeerc.org/bakken/completiontechnologies.aspx

Ge, J. and Ghassemi, A.. Analysis of failure potential around a hydraulic fracture in jointed rock. Presented at the 42nd U.S. Rock Mechanics Symposium (USRMS), 29 June-2 July, San Francisco, CA, ARMA 08-252, 2008.

Gorjian, M.. Investigation of the Geeomechanical Controls on Hydraulic Fracturing In the Bakken Formation, Southeast Saskatchewan. PhD. Thesis, University of Saskatchewan, CA, 2019.

560   Gorjian, M., Hawkes, C.D.. A workflow for analyzing stress shadow during hydraulic fracturing, with application to the Bakken Formation, southeast Saskatchewan, CSPG/CSEG/CWLS GeoConvention, Calgary, AB, 2017.

Hoek, E. and Brown, E.T.. Empirical strength criterion for rock masses. *J. of Geotech. Engg. Divn., ASCE*, **106** (GT9): 1013-1035, 1980.

Koning, E.J.L.. Fractured water injection wells - Analytical modeling of fracture propagation. Society of Petroleum Engineers
565   14684-MS, 1985.

Smith, M.B. and Montgomery, C.T.. Hydraulic Fracturing: Taylor & Francis, New York, NY, 2015.

Nagel, N. B., Zhang, F., Sanchez-Nagel, M. A., & Lee, B.. Evaluation of Stress Changes Due to Multi-Stage Hydraulic Fracturing – Consideration of Field Results. ISRM international symposium, Eurock, Wroclaw, Poland, 2013.

National Energy Board.. The Ultimate Potential for Unconventional Petroleum from the Bakken Formation of Saskatchewan
570   - Energy Briefing Note. National Energy Board of Canada and Saskatchewan Ministry of the Economy, 2015. https://www.neb-one.gc.ca/nrg/sttstc/crdlndptrlmprdct/rprt/2015bkkn/index-eng.html

Oilfield Geomechanics LLC.: Stress Shadows Explained: What it is, What it isn't, and Why you should care, 2015. http://www.ofgeomech.com/wp-content/uploads/2015/ 10/Stress_Shadows_Explained.pdf (Accessed May 2015)

Patterson, R. A.. Characterizing complex fracture geometry through data integration in the Permian basin. MSc. Thesis, Texas
575   A&M University, Austin, TX, 2017.

Perkins, T.K. and Gonzalez, J.A.. The effect of thermoelastic stresses on injection well fracturing. *SPE Journal* **25** (1): 78-88. DOI: 10.2118/11332-pa, 1985

Pollard, D.D. and Segall, P.. Theoretical displacements and stresses near fractures rock: With applications to faults, joints, veins, dikes, and solution surfaces. In Atkinson, B.K., ed., *Fracture Mechanics of Rocks*, New York: Academic Press, 1987.

580 Roussel, N. P.. Analyzing ISIP stage-by-stage escalation to determine fracture height and horizontal-stress anisotropy. SPE Hydraulic Fracturing Technology Conference and Exhibition, 24–26 January, The Woodlands, TX, SPE-184865-MS, doi:10.2118/184865-MS, 2017

Sheorey P.R.. *Empirical Rock Failure Criteria.* A.A Balkema Publishers, Old Post Road, Brookfield, U.S.A, 1997.

Suppachoknirun, T., & Tutuncu, A. N.. Hydraulic fracturing and production optimization in Eagle Ford shale using coupled

585 geomechanics and fluid flow model. *Rock Mechanics and Rock Engineering*, *50*(12), 3361-3378, 2017.

Warpinski, N. R.. Measurement of width and pressure in a propagating hydraulic fracture. *SPE Journal*, **25**(1), 46-54, 1985.

Zangeneh, N.. Numerical simulation of hydraulic fracture, stress shadow effects and induced seismicity in jointed rock. PhD. thesis, Faculty of Geological Engineering, The University of British Columbia, Vancouver, BC, 2013.

Zoback, M. D.. *Reservoir Geomechanics*. Cambridge Univeristy Press, New York, NY, 2007.

590

595

600

605

Appendix A Thermo-elastic Stress

For analyzing the thermo-elastic stress shadow effect, the parameters given in Table A.1 were used. For analyzing the influence of a non-uniform temperature distribution around the fracture (rather than the uniform temperature assumed by Perkins and Gonzalez (1985), the heat transfer Equation A.1 was solved numerically by using finite difference method.

$$\rho c_p \frac{\partial T}{\partial t} = \nabla . (\lambda \nabla T) \tag{A.1}$$

Where λ = thermal conductivity

ρc_p = heat capacity per unit volume

The modeled temperature distribution by using the finite difference method and by Perkins and Gonzalez (1985) for a single fracture is shown in Figure A.1. For a maximum injection volume scenario of 11 tonnes of proppant and injection time of 75 minutes per stage a_0 = 52 m and b_0 = 0.049 m for the cool region.

The major axis of the elliptical cool region has almost the same length as fracture length with time. Figure D.2 shows the therm-elastic stress shadow perpendicular and parallel to fracture. According to Figure D.2, the minimum thermos-elastic stress shadow in X-direction is 21.6 MPa. Due to Equation D.2, it was not expected to see secondary thermal fractures during the hydraulic fracture treatment, as the original horizontal stress in X direction (σ_X) plus the thermos-elastic stress shadow is still more than tensile strength of rock.

$$\sigma_X + \Delta\sigma_{TX} \geq -\sigma_t \tag{A.2}$$

Where σ_X = maximum horizontal stress

$\Delta\sigma_{TX}$ = thermo-elastic stress shadow in X direction

σ_t = tensile strength, with negative sign, that is mostly assumed zero

Table A.1. Input parameters used for analyzing thermo-elastic stress shadow

Injection condition	
Depth to the center of the formation (D)	1615 m
Reservoir thickness (h)	7.2 m
Water injection rate (Iw)	0.65 m^3/min
Time (t)	47 minutes
Initial Reservoir temperature (TR)	65°C
Bottomhole temp. of the injection water (Tw)	21.1°C
Reservoir Rock Properties	
Compressibility of grains (Cgr)	5.43E-05 $(MPa)^{-1}$
Compressibility of formation (Cf)	6.00E-05 $(MPa)^{-1}$
Young's modulus (E)	25 GPa
Relative perm. To water (Krw)	0.29
Residual oil saturation (Sor)	0.25
Initial water saturation (Swi)	0.2
Linear coefficient of thermal expansion (α)	10.5E-06 mm/(mm*K)
Specific heat of mineral grains per unit volume (ρCP)	1.662 $MJ/m^3 * K$
Thermal conductivity (λ)	2.458 W/(m*K)
Poisson's ratio (υ)	0.25
Reservoir permeability (k)	0.1 md
Porosity (φ)	0.11
Reservoir Fluid Properties	
Viscosity of oil at 65°C (μo)	1.47E-09 Mpa*s
Viscosity of oil at 65°C (μwhot)	4.30E-10 MPa*s
Viscosity of oil at 21°C (μwcold)	9.95E-10 MPa*s
Compressibility of oil (co)	1.50E-03
Compressibility of water (cw)	5.20E-04 $(MPa)^{-1}$
Specific heat of oil (Co)	2.1 KJ/(kg*K)
Specific heat of water (Cw)	4.2 KJ/(kg*K)
Density of oil (ρo)	810 kg/m^3
Density of water (ρw)	1180 kg/m^3

640

(a)

(b)

Legend
Horizontal well:
Hydraulic Fracture:
(viewed from above)
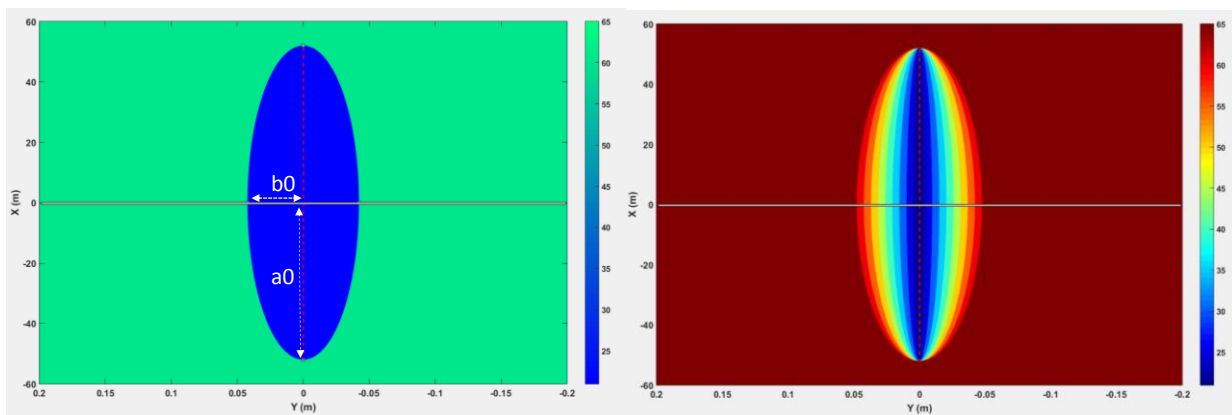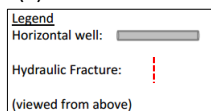
Figure A.1: Temperature distribution (°C) and cool region (major axis of a_0 and minor axis of b_0 shown on the Figure D.1(a) by white dashed arrow) around the hydraulic fracture (demonstrated by red dashed line in center) predicted using (a) Perkins and Gonzalez (1985) method and (b) the finite difference approach.

(a)

(b)

Legend
Horizontal well:
Hydraulic Fracture:
(viewed from above)
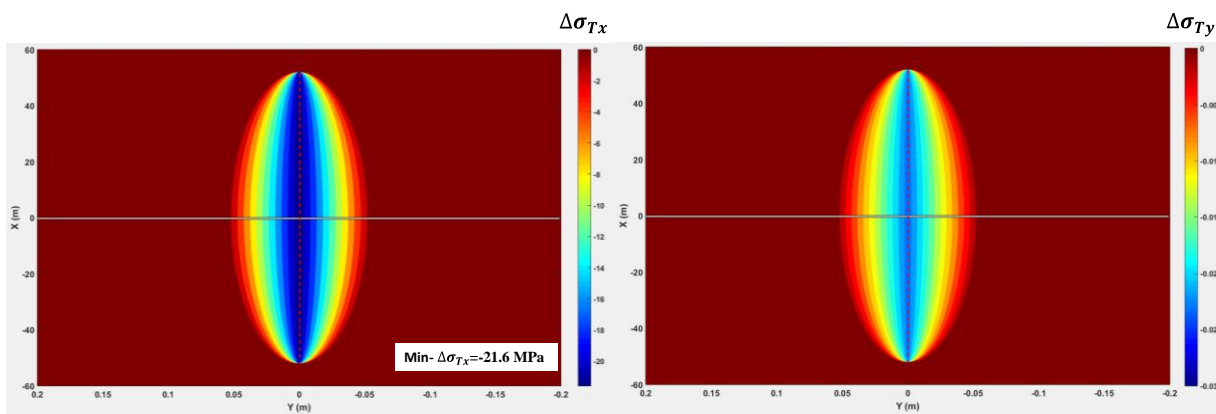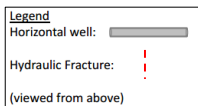
Figure A.2: Predicted thermo-elastic stress shadow in (a) X direction and (b) Y direction in MPa

Appendix B: Poro-elastic Stress

For analyzing poro-elastic stress shadow, parameters given in Table A.1 were used. By assuming an injection time of 47 minutes and a permeability of 0.1 md, the poro-elastic stress is negligible. However, by assuming an injection time of 75

655 minutes, and increasing the permeability to 2.5 md, the pore pressure distribution is simulated with results shown in Figure B.1. For this injection time, 2.5 md seems to represent a permeability threshold. Any permeability lower than that gives rise to negligible pore pressure change around the fracture. For a maximum injection volume scenario of 11 tonnes of proppant and injection time of 75 minutes per stage $a_1 = 52.001$ m and $b_1 = 0.33$ m for the flood region.

The major axis of the elliptical flood region has almost the same length as fracture length with time. Figure B.2 shows the

660 poro-elastic stress shadow perpendicular and parallel to the fracture.
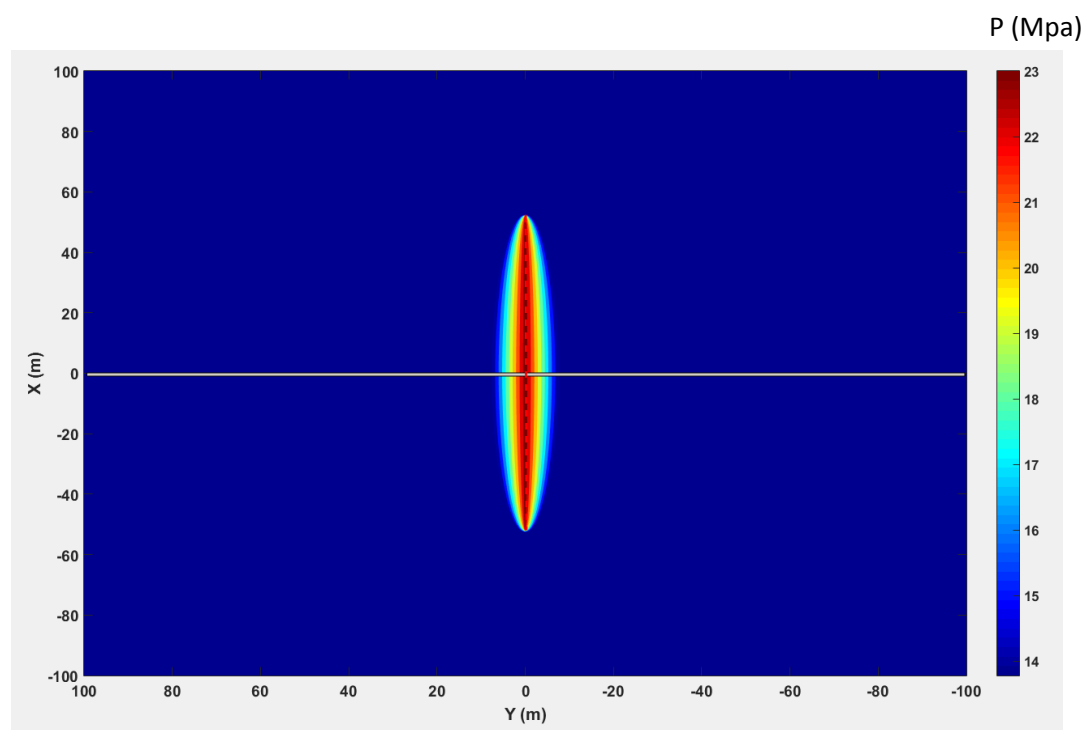
Figure B.1: Pore pressure distribution (MPa) around hydraulic fracture after 75 minutes of injection and assuming a reservoir permeability of 2.5 md.
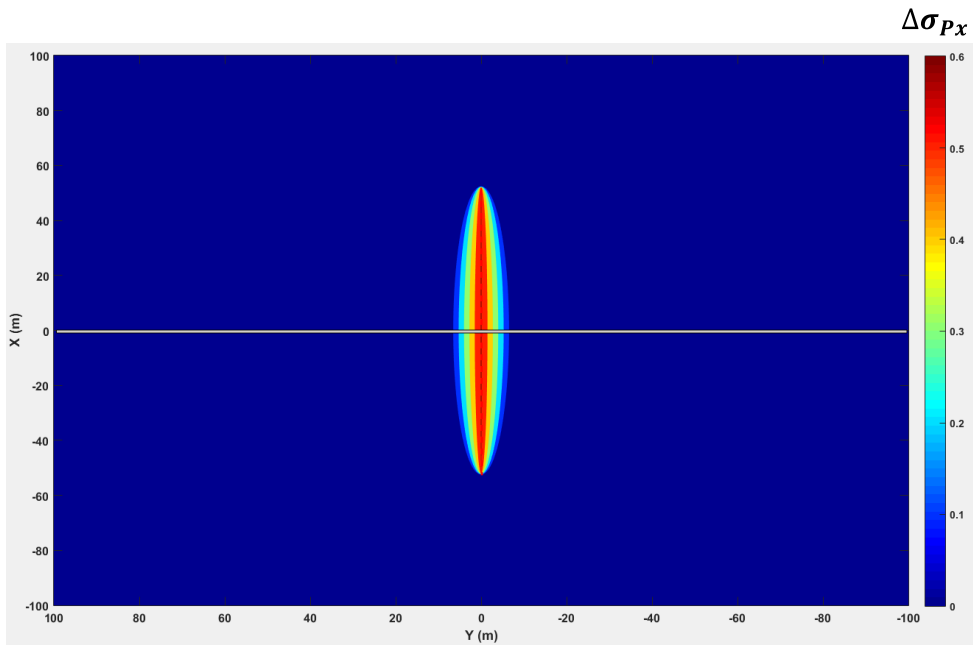
665   (a)
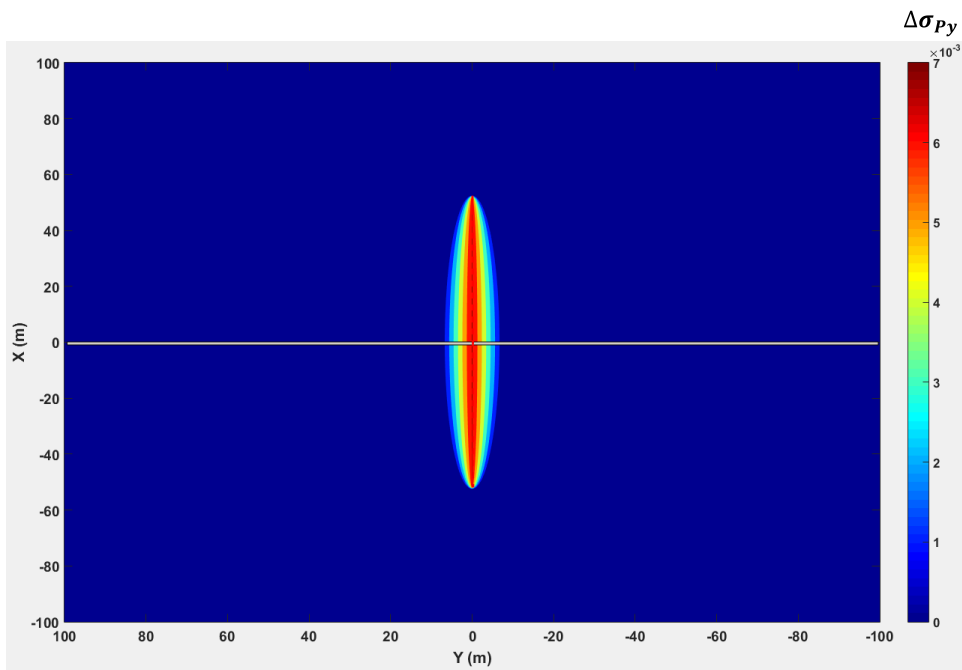
(b)

Figure B.2: Predicted poro-elastic stress shadow in (a) X direction and (b) Y direction in MPa

Appendix C Microseismic events in well L
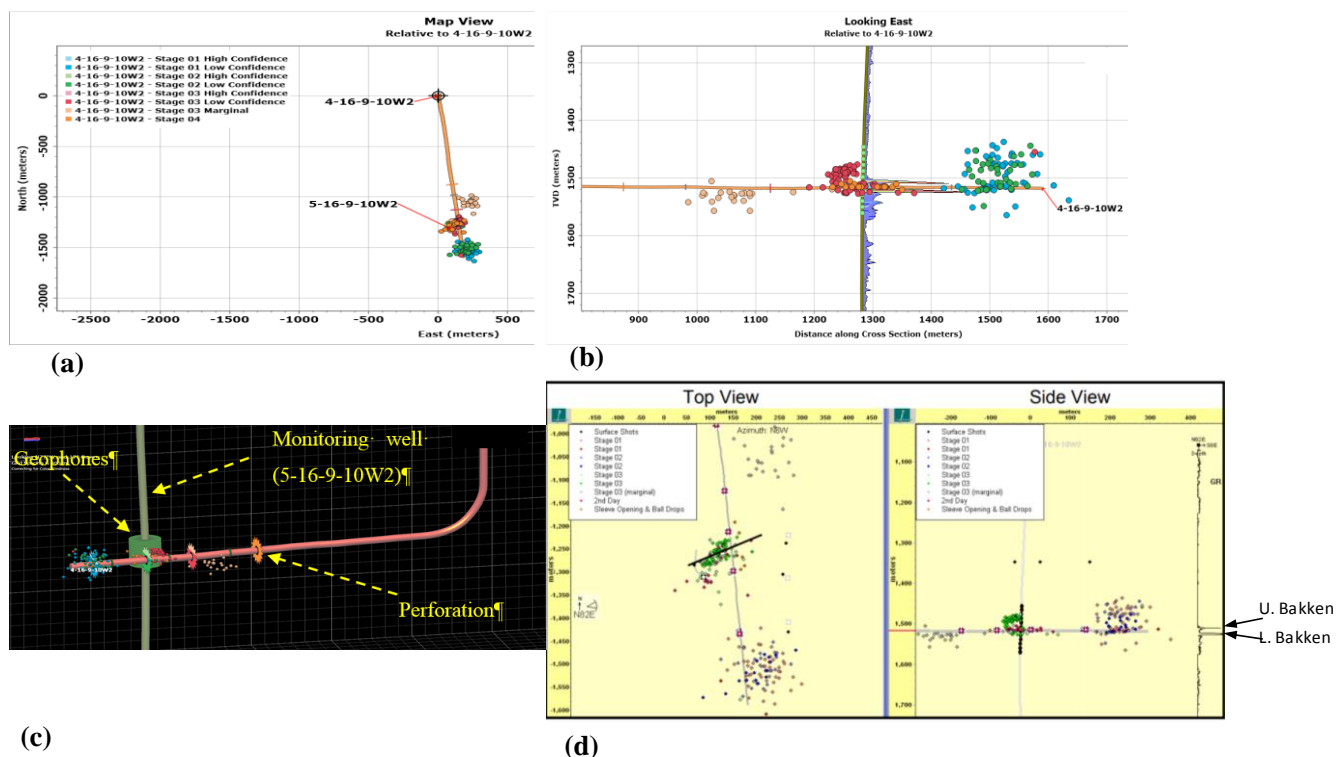
670

Figure C.1: Microseismic events during hydraulic fracturing of well 5-16-9-10W2 (a) Top view generated by the author using data provided by the well operator, (b) side view generated by the author, (c) 3D view generated by the author, and (d) original top and side views by Kendall (2009). Note significant growth vertically out of zone, both up and down, and a stimulated zone half-length of roughly

675